Systems Engineering of the Global L-Band Observatory for Water Cycle Studies

James Nathan Smith

A thesis submitted to the faculty of
Brigham Young University
in partial fulfillment of the requirements for the degree of

Master of Science

David G. Long, Chair
Willie K. Harrison
Brian D. Jeffs
Michael J. Wirthlin

Department of Electrical and Computer Engineering

Brigham Young University

ABSTRACT

Systems Engineering of the Global L-Band Observatory
for Water Cycle Studies

James Nathan Smith
Department of Electrical and Computer Engineering, BYU
Master of Science

The Global L-band Observatory for Water Cycle Studies (GLOWS) is designed as a follow-on to the Soil Moisture Active Passive (SMAP) observatory launched in 2015. While GLOWS is essentially copying many aspects of the SMAP mission, a key change has been made in the antenna technology. SMAP uses a reflector antenna and to reduce mission costs GLOWS uses a metamaterial lens antenna. This type of antenna is less efficient, so it must be proven that GLOWS can achieve the same uncertainty levels in soil moisture measurements as SMAP. In this work, a unified framework for modeling and analyzing GLOWS' ability to meet all mission and measurement requirements is developed. A model for the uncertainty effects of the lens antenna is developed and used to show that so long as the lens efficiency is above a threshold determined by the accuracy of the lens physical temperature knowledge, GLOWS will also be able to achieve all measurement requirements. It is shown that GLOWS is able to copy the design parameters of SMAP and achieve the same mission requirements.

Keywords: remote sensing, soil moisture, radiometry, lens antenna

ACKNOWLEDGMENTS

This thesis would not have been possible without the support of many people:

To my professors, especially Dr. Long, thank you for the efforts you put into teaching. I have enjoyed every one of my classes and feel like they have prepared me well for the adventures ahead.

To Andrew Santa and Jacob Stratford, thank you for all of the help you gave me in working on the geometry code. Making sure we all had our reference frames straight was difficult, but you helped make it happen.

To my friends and labmates, especially Nate Porter, Josh Kjar, Adam Whipple, and Tayler Livingston, thank you for helping me in classes while I was so busy working on this thesis. I am going to miss working with you. Best of luck as you continue your work.

To my parents and siblings, thank you for being the constant in my life and for helping me have so many opportunities to learn what I want to do.

To my wife Aubrie, thank you for putting up with my endless work and for helping me get it done. Your support made this all possible. I am so excited for our next adventures together.

This work has been supported by the National Aeronautics and Space Administration (NASA) under contract NASA 80NSSC20K0319.

TABLE OF CONTENTS

LIST OF FIGURES

CHAPTER 1. INTRODUCTION

1.1 Remote Sensing and the SMAP Mission

Remote sensing is the act of measuring something from a distance. These measurements are generally taken from some portion of the electromagnetic spectrum. In the BYU Microwave Earth Remote Sensing (MERS) Lab, we work with sensors and data that operate in the microwave region between about 1 and 100 GHz. Over the last several decades, microwave remote sensing instruments flown aboard spacecraft have become crucial to humanity's understanding of the environment.

Microwave instruments include both active (radar) and passive (radiometer) categories [1]. Radars (originally from the acronym RAdio Detection And Ranging) transmit a burst of microwave energy and measure characteristics of the echo to determine characteristics of the target it reflects from. This can include both detecting the presence of an object and measuring the distance (range) to it as radar was originally used for, but can also include size, roughness, or several other geophysical parameters that affect the echo. Radars can also be used to image a surface by combining multiple measurements using an approach known as synthetic aperture radar (SAR). In contrast to radars which transmit and receive, radiometers are passive sensors that only observe microwave emissions from the target. These emissions include reflections from other sources and the emissions that every object naturally radiates. Measurements of this radiation can also be used to estimate characteristics of the radiating body. Depending on the application, one or a combination of these instruments can be used to take the most useful measurements to estimating the parameter of interest.

In the case of the Soil Moisture Active/Passive (SMAP) mission which was developed by the Jet Propulsion Laboratory (JPL) and launched in January 2015, the primary parameter of interest is global soil moisture levels. However, many other applications have been

developed. SMAP contains both an L-band radar (active) and L-band radiometer (passive). The radiometer measurements tend to be more accurate and precise but have less resolution, while the radar which can be operated in a SAR mode provides higher resolution. Both sets of data can be combined to produce soil moisture measurements that are high resolution and have low uncertainty. The soil moisture measurements have proven useful in several areas such as weather and climate forecasting, drought and flood monitoring, and agricultural productivity [2]. Unfortunately, after a few months in orbit, a component in the amplifier for the radar failed and SMAP could only collect passive radiometer measurements [3]. Thanks in part to reconstruction algorithms that enhance the radiometer measurement resolution [4], the radiometer soil moisture measurements have continued to be extremely useful. At this point, SMAP has long outlived its planned three year mission lifetime and a replacement must be developed before the radiometer also fails to continue logging the soil moisture data.

1.2 The GLOWS Mission

The Global L-Band Observatory for Water Cycle Studies (GLOWS) is the mission tasked with replacing SMAP [5]. In most respects, GLOWS can essentially copy the design of SMAP, especially in the orbit selection and measurement methodology to ensure that the measurements are taken in the same way. However, key changes can be made in the technologies used to make GLOWS smaller and cheaper, especially by reducing the cost of launch with a smaller satellite.

The largest such change is the choice of antenna. SMAP used a six meter deployable parabolic reflector antenna which deflected the antenna beam off at a 35 degree angle from the nadir direction. This antenna mechanism required a complicated deployment and an even more complicated system for balancing the spacecraft while the antenna is rotated. GLOWS, on the other hand, will make use of a multi-layered metamaterial lens antenna. This antenna utilizes resonant copper patches on each layer of substrate which deflect the antenna beam off at the same 35 degree angle from nadir, but allows the mechanical structure to be simplified. The lens can be packed much more compactly than the reflector and its deployment is more straightforward. Positioning the lens directly underneath the spacecraft

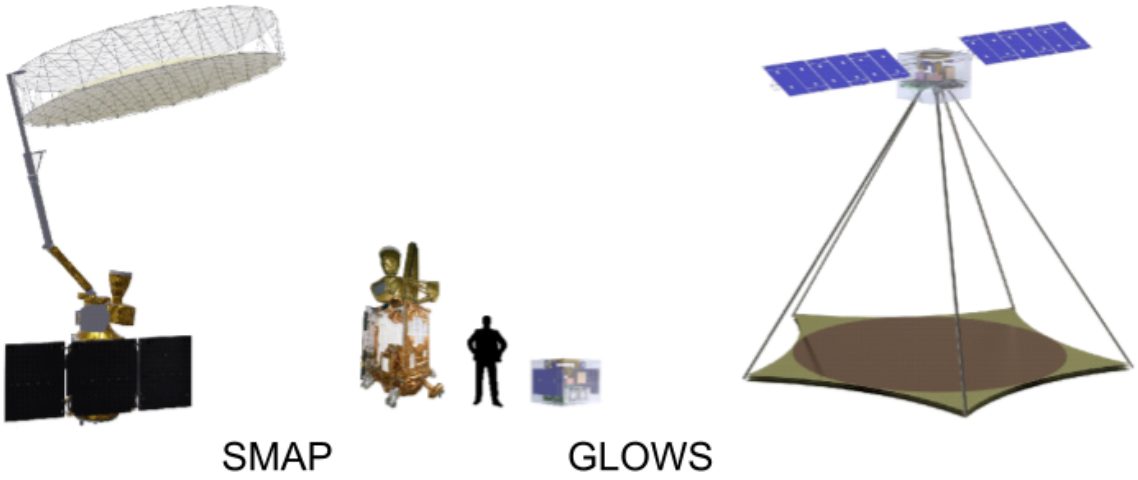

Figure 1.1: Visual comparison of SMAP and GLOWS. Note especially the difference in the antennas and more compact stowed volume [5].

with the mass evenly distributed also significantly simplifies the systems needed to balance the spacecraft as the antenna rotates.

1.3 Problem Definition, Contributions, and Thesis Overview

Although the GLOWS mission copies the majority of the SMAP mission to ensure that the collected data is as similar as possible, it is being developed by a different team. SMAP, as mentioned previously, was developed at JPL, while GLOWS is being developed by a team comprised of groups at Brigham Young University (BYU), Goddard Space Flight Center (GSFC), MMA Design LLC (MMA), and Agile RF Systems LLC (ARS). While this team has access to the original SMAP mission requirements documentation, it would like to create a unified and consolidated package including more justification. To that end, a framework for modeling the mission has been developed and used to justify the key mission requirements.

In addition to validating the mission requirements, the team must be prove that the GLOWS instruments can achieve similar performance to the SMAP instruments. While the switch to a lens antenna dramatically simplifies the mechanical design, such an antenna has never before been used in a spaceborne remote sensing mission. As such, the performance of this antenna and its effects on microwave instruments have not been fully characterized.

Because the signal must pass through the antenna rather than being reflected off of it, the antenna is guaranteed to be less efficient to some degree. The key question is whether this loss of efficiency will cause the uncertainty in the radiometer measurements to exceed that required to achieve desired uncertainty in the soil moisture estimates. This is done by developing a model for the analysis of the radiometric performance of the lens and simulating its effects on the overall performance of the radiometer. The performance of the radar is assumed to be negligibly affected because it requires much less sensitivity and the transmit power can be increased to account for the increased loss through the antenna. The radiometer has no such possible remedies.

The overall goal of this work is to validate the ability of the GLOWS mission to meet the same requirements as SMAP. In so doing it is found that the mission requirements developed for SMAP are justifiable. It is also found that while the loss through the lens has the potential to degrade the performance of the lens, understanding its properties allows its effect to be ameliorated, so the instrument will be able to meet the mission performance requirements.

1.3.1 Contributions

In performing this work, the following contributions are made:

1. Improvement of observational geometry modeling
2. Verification that orbit and observation geometry meet mission requirements
3. Validation of the connection between soil moisture and brightness temperature uncertainties
4. Development of a radiometric model of a lens antenna
5. Determination that the radiometer can still meet performance requirements despite loss in antenna efficiency

1.3.2 Overview

The rest of the thesis explains each of these contributions. Chapter 2 provides some background on radar, radiometry, and the SMAP mission requirements and concept of operations which GLOWS will strive to match. Chapter 3 details the geometry and orbit modeling. Chapter 4 explains the methodology used to ensure that GLOWS meets key mission requirements. In Chapter 5 the radiometric model of the lens antenna is derived and used to validate the performance of the radiometer. Chapter 6 contains conclusions and suggestions for future work.

CHAPTER 2. BACKGROUND ON MICROWAVE INSTRUMENTS AND SMAP

In this chapter, the basics of active and passive microwave instruments and the basic requirements and concept of operations of the SMAP mission are defined as important background to understanding the GLOWS mission. First, a brief overview of radars, which are active microwave instruments, is provided. Second, an overview of passive radiometer sensors is provided. More detail about radiometers is provided because most readers are less familiar with the functionality of these instruments compared to radars. Finally, a high-level overview of the SMAP mission allows the reader to understand what it is that the GLOWS mission is trying to accomplish by replicating the key elements of SMAP.

2.1 Active: Radar

Radars transmit microwave energy and measure the reflections of that energy off of target objects to determine various characteristics of the objects. These characteristics can include detecting whether an object is present, measuring distance to the object, measuring the velocity of the object, determining the approximate size of the object, or any of several other characteristics so long as a model has been created for extracting information about the characteristic from the returned energy. Synthetic aperture radars (SARs) are specialized radar sensors that image surfaces by dividing the returned energy from several pulses using the time delay and Doppler shifts caused by different points in view of the radar [1].

All radars make use of the radar range equation [1]

$$P_r = \frac{P_t G_t G_r \lambda^2 \sigma}{(4\pi)^3 R^4}, \tag{2.1}$$

where P_r is the received power in Watts, P_t is the transmitted power in Watts, G_t is the gain of the transmitting antenna, G_r is the gain of the receiving antenna, λ is the wavelength of

the radar pulse, σ is the radar cross section of the object, and R is the range (or distance) to the object. If the radar is looking at a distributed area (i.e., the Earth's surface) rather than a single object, σ is replaced with σ_0 which is the normalized radar cross section. This is the typical application for a radar in remote sensing. Usually, everything except σ_0 is known or can be easily calculated, so the equation is rearranged to solve for σ_0 which carries the information about the physical properties of the region of interest (roughness, material, etc.). An accurate model (that may or may not require some ancillary data) may be used to convert from the measured σ_0 to the property of interest.

2.2 Passive: Radiometry

Radiometry is the act of passively measuring microwave emissions which emanate from all physical objects warmer than zero degrees Kelvin. These measurements can be taken from a satellite in space of the Earth or of space from the Earth. The latter is generally termed radio astronomy. In either case, the measured quantities are extremely small. Thus, radiometer instruments must be precise and well calibrated. This section briefly covers the basics of radiometry; for a more detailed treatment of the subject, see Chapters 6 and 7 of [1].

2.2.1 Thermal Radiation

The radiation emanated from all physical objects is caused by transitions of electrons between energy levels in atoms. As taught in most introductory chemistry classes, when an electron transitions to a lower energy state it releases the energy as radiation at a frequency determined by the energy difference between the states. Conversely, if radiation of the same frequency hits an atom, that energy can be absorbed and cause a transition from the lower to the higher state.

The spontaneous radiation as a result of electron transitions is caused when atoms collide. The rate at which atoms collide is determined by the kinetic energy of the atoms, which is defined by the absolute temperature of the atoms. The absolute temperature of a substance is therefore directly tied to the radiation which it emits. This relationship

is described by Planck's Blackbody Radiation Law. A blackbody is a hypothetical ideal material which absorbs all incident radiation. In contrast, real materials reflect some fraction of incident radiation. If the blackbody is in thermodynamic equilibrium, it must emit as much energy as it absorbs, so a blackbody is a perfect absorber and a perfect emitter. Planck's Blackbody Radiation Law defines the spectral brightness intensity, or the amount of power that a blackbody radiates in all directions,

$$I_f = \frac{2hf^3}{c^2}\left(\frac{1}{e^{hf/kt}-1}\right), \tag{2.2}$$

where I_f is the spectral brightness (or specific) intensity in $\mathrm{Wm^{-2}Hz^{-1}sr^{-1}}$, h is Planck's constant (6.63×10^{-34}J·s), f is frequency (Hz), k is Boltzmann's constant ($1.38\times10^{-23}\mathrm{JK^{-}}1$), T is the blackbody's absolute temperature (K), and c is the speed of light in a vacuum (3×10^8 m/s). This equation is illustrated in Fig. 2.1 at several temperatures and over a wide range of frequencies. As the temperature increases, it is seen that the energy in the higher frequencies increases through the optical region and into the x-ray region as seen by heating an object up. It is also apparent from the figure that even at relatively low temperatures, there is still power (albeit at quite low levels) in the microwave spectrum. While Planck's Blackbody Radiation Law varies significantly over frequency, for a sufficiently bandlimited observation, the thermal radiation can be approximated as constant over frequency. In this case the power emitted by a blackbody (P_{bb}) is given as

$$P_{bb} = kTB, \tag{2.3}$$

where B is the bandwidth of the observation (Hz).

Real materials (sometimes called gray bodies) are not perfect absorbers or emitters. The radiation emitted by a gray body may be dependent on direction and is less than that which would be emitted by a blackbody at the same temperature. The ratio of the spectral brightness intensity of a real material to that of a blackbody is known as its emissivity:

$$e(\theta,\phi) = \frac{I_f(\theta,\phi)}{I_{bb}}, \tag{2.4}$$

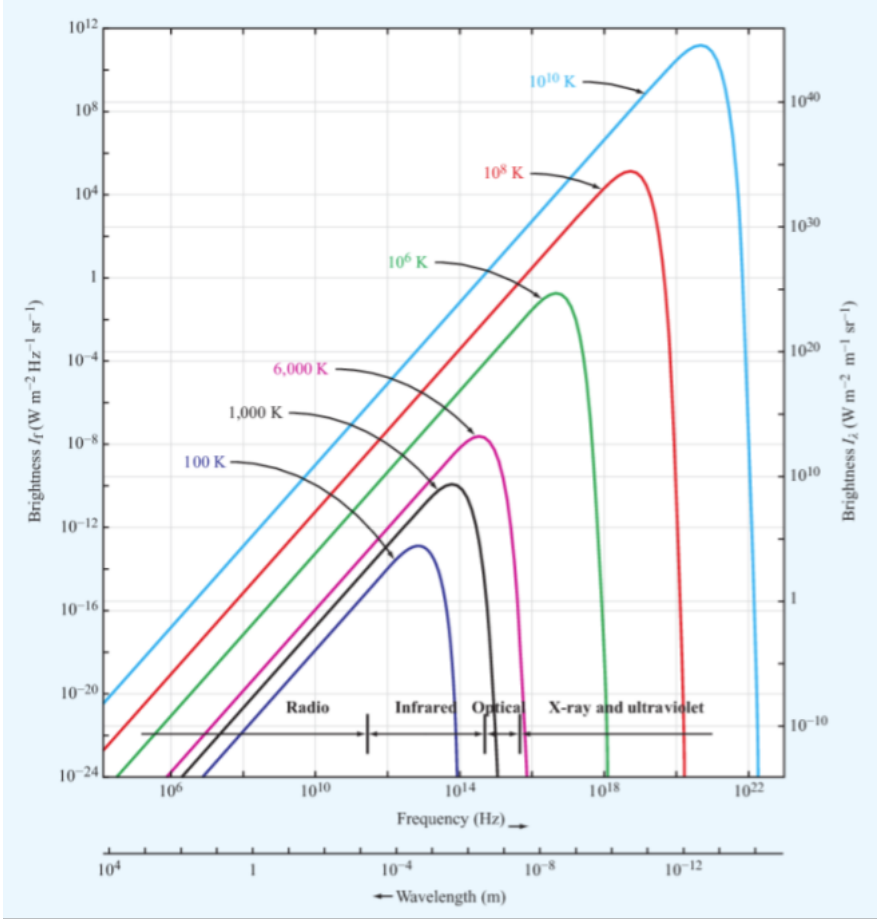

Figure 2.1: Planck's Blackbody Radiation Law evaluated at several temperatures over a large portion of the electromagnetic spectrum. Taken from [1].

where $e(\theta, \phi)$ is the emissivity by direction, $I_f(\theta, \phi)$ is the spectral brightness intensity of the real material by direction, and I_{bb} is the spectral brightness intensity of a blackbody at the same absolute temperature. Another way of relating the two is by the equivalent brightness temperature (T_B) to a blackbody of the real material

$$T_B = e(\theta, \phi)T, \tag{2.5}$$

where T is the absolute physical temperature of the material (K).

The relationship of emissivity and temperature to an equivalent blackbody temperature allows for the use of radiometer measurements in estimating properties of different materials. Knowing Boltzmann's constant and the bandwidth of a measurement, T_B can be

calculated from the power of the measurement by Eq. 2.3. Then, by knowing the absolute temperature of the material, Eq. 2.5 can be used to estimate the emissivity of the material. The emissivity is related to many geophysical parameters of the material, so depending on the parameter desired to be estimated, provided the correct model of the relationship between the parameter and the emissivity, the parameter can be derived from the estimated emissivity.

2.2.2 Radiometer Signal Flow

To derive physical parameters from radiometer measurements, the relationship between the observed power of the emitted radiation from the material and the actual output power of the radiometer must be understood. The observed power is altered by several losses and gains as it passes through the antenna, amplifiers, and filters that all make up the radiometer system. The effects of each component must be characterized in order to determine the total effect of the system on the received power and be able to remove the system's effects from the measurement and be left with only the observed power. Also, because the quantity of interest is actually the brightness temperature of the observation, the power is generally represented just by the temperature equivalent to that power from Eq. 2.3. This convention is followed throughout the rest of this section.

The first component to observe the power emitted by the material is the antenna. The antenna integrates power from all directions, weighted by the antenna gain pattern. Knowledge of its gain pattern and the expected power from all directions other than the region of interest is necessary in order to constrain the measurement to only the region of interest. The total observed brightness temperature by the antenna (T_A) is a weighted average of the brightness temperature observed from all directions by the antenna's gain pattern defined by

$$T_A = \frac{\iint\limits_{4\pi} T_B(\theta,\phi)G(\theta,\phi)\,d\Omega}{\iint\limits_{4\pi} G(\theta,\phi)\,d\Omega}, \tag{2.6}$$

where $T_B(\theta,\phi)$ is the brightness temperature observed in a given direction and $G(\theta,\phi)$ is the antenna gain pattern. The antenna also adds some noise power dependent on its radiometric

efficiency (ξ), so the total brightness temperature out of the antenna $T_A^{'}$ is defined by

$$T_A^{'} = \xi T_A + (1 - \xi) T_p, \tag{2.7}$$

where T_p is the physical temperature of the antenna.

$T_A^{'}$ is the equivalent brightness temperature of the power delivered by the antenna to the rest of the radiometer system. From there the signal is passed through several amplifiers, filters, and other RF components before it is finally digitized and sampled. Each component adds noise to the signal. The effect of this noise can be modeled as an equivalent bias to the measured input power. This bias in terms of brightness temperature is called equivalent input noise temperature (T_E) and is given by

$$T_E = (F - 1) T_0, \tag{2.8}$$

where F is the noise figure of the component and T_0 is the standard reference temperature of 290 K (because the noise figure is defined at T_0). If a component is passive, the noise figure is equivalent to the reciprocal of the loss (L^{-1}). For lossy devices, T_0 must be replaced with the physical temperature of the device. The T_Es of N cascaded components can all be referred to the input of the first component to determine the overall equivalent input noise temperature by the following relationship

$$T_E = T_{E_1} + \frac{T_{E_2}}{G_1} + \frac{T_{E_3}}{G_1 G_2} + \cdots + \frac{T_{E_N}}{G_1 G_2 \ldots G_{N-1}}, \tag{2.9}$$

where T_{E_i} and G_i are, respectively, the equivalent input noise temperature and gain of the ith component. Given all of the details of the components of a radiometer receiver, this relationship can be used to determine the equivalent input noise temperature of the receiver T_{REC}. Combining T_{REC} with $T_A^{'}$ yields the equivalent input temperature of the entire system:

$$T_{\mathrm{SYS}} = T_A^{'} + T_{\mathrm{REC}}, \tag{2.10}$$

which is the equivalent brightness temperature that is actually seen by the radiometer receiver.

2.2.3 Measurement Uncertainty and Calibration

The ultimate goal of the radiometer is to report the brightness temperature of the region of interest in view of the mainlobe of the antenna. As with all measured quantities, there are two aspects to the uncertainty of the reported T_B measurements: accuracy and precision. Accuracy is a measure of how far the average of the measurements is from the truth while precision is a measure of the spread of multiple measurements of the same quantity. The accuracy of the measurements depends on the accuracy of all the quantities used in converting from the measured voltage/power to T_B. Any bias in those quantities introduces a bias in T_B. Radiometric precision is determined by the architecture of the radiometer system. For an ideal total power radiometer, the precision is defined as

$$\Delta T_{\mathrm{SYS}} = \frac{T_{\mathrm{SYS}}}{\sqrt{B\tau}}, \tag{2.11}$$

where ΔT_{SYS} is the standard deviation of the measured value of T_{SYS}, B is the radiometer bandwidth, and τ is the radiometer integration time. Adding and subtracting deterministic values from the estimate of T_{SYS} to remove bias and determine T_B does not affect the standard deviation, but any scaling does. However, since scaling done to account for the attenuation of the antenna is close to unity, ΔT_B is generally very close to ΔT_{SYS}. This ideal ΔT_{SYS} is the lowest precision possible for a radiometer. Gain fluctuations can also affect the precision, but certain radiometer architectures can minimize the gain fluctuation to prevent that to varying degrees. The details of the precision achieved by other architectures can be found in Chapter 7 of [1].

In terms of accuracy, all of the quantities involved in extracting T_B from T_{SYS} must be considered. This process requires working backwards from T_{SYS}, subtracting T_{REC} from T_{SYS} to get T_A', subtracting out the added noise by the antenna and accounting for the efficiency scaling in Eq. 2.7, and finally subtracting out the expected brightness temperature from the sidelobes in Eq. 2.6. Each of these steps requires accurate knowledge of the quantities

being subtracted or scaled to avoid biasing the resultant T_B measurement. Achieving this knowledge is done by calibration. The radiometer receiver is usually calibrated against a known load by use of a switch placed between the antenna and receiver. The brightness temperature of the load replaces $T_A^{'}$ in Eq. 5.3 and allows T_{REC} to be determined from the measurement. This process is generally done quite frequently during the operation of the radiometer to prevent gain and temperature fluctuations from affecting the measurements too greatly. Because of this repeated and detailed calibration, the accuracy of $T_A^{'}$ is high.

Accurately going from $T_A^{'}$ to T_B raises several uncertainty issues. Most antennas used for radiometers have very high radiometric efficiency which prevent the antenna from adding very much noise. This minimizes many of the uncertainty concerns. In the case of GLOWS, however, the lens antenna has lower radiometric efficiency and therefore its noise added by self emission is more sensitive to the antenna physical temperature. Characterizing the uncertainty involved in this process is a main focus of Chapter 5.

2.3 SMAP Mission

The Soil Moisture Active Passive (SMAP) mission, was launched in January 2015 to measure global soil moisture. The mission came about in response to the National Research Council's Decadal Survey commissioned by NASA which found that soil moisture is a key factor in several areas of research [2]. SMAP was designed to help provide accurate measurements of soil moisture for use in all of these research areas. In order to measure soil moisture, SMAP contains both an L-band radar and an L-band radiometer (hence the Active Passive part of the mission name). Unfortunately the radar on SMAP failed after about 6 months in orbit [3], so the mission has been forced to rely solely on the radiometer measurements and cannot meet all of the original requirements. The rest of this section details the SMAP mission requirements and the key design parameters of the mission sensors.

2.3.1 Requirements

In order to provide useful soil moisture measurements, the measurements must have sufficiently high resolution both temporally and spatially. To ensure this, several key mission

requirements for SMAP are specified. These requirements are summarized in Fig. 2.2. Temporally, the soil moisture measurements are required to be taken at a consistent time of day (6 AM/6 PM) and every 3 days or more frequently. The minimum desired spatial resolution is 40 km for hydroclimatology (larger scale analysis), but 10 km for hydrometeorology (more local, small-scale analysis). In terms of accuracy, the soil moisture measurements must be within $\pm 0.04 \text{cm}^3\text{cm}^{-3}$ of the truth in the top 5 cm of soil for areas with vegetation water content ≤ 5 kg per square meter. The requirements table in Fig. 2.2 also includes requirements on measuring freeze/thaw state which is necessary because frozen ground has different microwave characteristics than thawed ground and the soil moisture algorithm will not work in frozen areas. The SMAP radar is required to measure the freeze thaw state of land above 45° N (the Boreal region) at 3km spatial resolution every 2 days with 80% classification accuracy.

The measurement requirements are translated into instrument requirements on the right side of Fig. 2.2. To achieve the desired temporal resolution, it was determined that the swath width (the width of the area that the instruments can see at any given point in the orbit) must be 1000 km at the chosen orbit altitude of 685 km. The spatial resolutions require the resolution of the instrument measurements to meet the same requirements. For the radiometer, this means that the antenna main beam footprint size must be less than or equal to approximately 40 km, while for the SAR this means that various parameters must be chosen such that processed SAR resolution is less than 3 km for the freeze/thaw state measurements. The soil moisture accuracy requirements translate to 1.3 K uncertainty in T_B and 0.5 dB uncertainty in σ_0.

2.3.2 Instrument Design

In order to have achieve 40 km resolution in the radiometer measurements, the antenna has a beamwidth of 2.7°. Covering the entire 1000 km swath width requires scanning the antenna across the swath. A rotating scan was selected in order to maintain a constant incidence angle for the radar. The selected incidence angle is 40° which requires the antenna to have a look angle of 35° off of nadir at the 685 km orbital altitude. The antenna rotates at 14.6 rpm to maintain a spacing of about 31 km between successive scans near the center

Scientific Measurement Requirements	Instrument Functional Requirements
Soil Moisture: ~±0.04 cm^3cm^{-3} volumetric accuracy in the top 5 cm for vegetation water content ≤ 5 kg m^{-2} Hydrometeorology at ~10 km resolution Hydroclimatology at ~40 km resolution	**L-Band Radiometer (1.41 GHz):** Polarization: V, H, 3rd and 4th Stokes Parameters Resolution: 40 km Radiometric Uncertainty*: 1.3 K **L-Band Radar (Tunable from 1.22–1.3 GHz):** Polarization: VV, HH, HV (or VH) Resolution: 10 km Relative accuracy*: 0.5 dB (VV and HH) Constant incidence angle** between 35° and 50°
Freeze/Thaw State: Capture freeze/thaw state transitions in integrated vegetation-soil continuum with two-day precision, at the spatial scale of landscape variability (~3 km).	**L-Band Radar (Tunable from 1.22–1.3 GHz):** Polarization: HH Resolution: 3 km Relative accuracy*: 0.7 dB (1 dB per channel if 2 channels are used) Constant incidence angle** between 35° and 50°
Sample diurnal cycle at consistent time of day (6 AM/6 PM equator crossing) Global, ~3 day (or better) revisit Boreal, ~2 day (or better) revisit	Swath width: ~1000 km Minimize Faraday rotation (degradation factor at L-band)
Observation over minimum of three annual cycles	Baseline 3-year mission life

* Includes precision and calibration stability ** Defined without regard to local topographic variation

Figure 2.2: Requirements on the SMAP mission and instruments. Taken from [6].

of the swath. The reflector, feed, and radiometer electronics are all rotated, while the radar electronics are on the de-spun side.

The polarimetric radiometer measures the brightness temperature at horizontal and vertical polarizations as well as the third and fourth Stokes parameters. It operates at a center frequency of 1.4135 GHz with a bandwidth of 24 MHz. The electronics of the radiometer are represented in the block diagram in Fig. 2.4. The horizontal and vertical polarizations come out of the orthomode transducer (OMT), while the third and fourth Stokes parameters are calculated using the digitized horizontal and vertical samples. The antenna pattern on the ground from the radiometer is termed a footprint. One radiometer footprint measurement contains 12 packets of downlinked data which each contain the integration of the

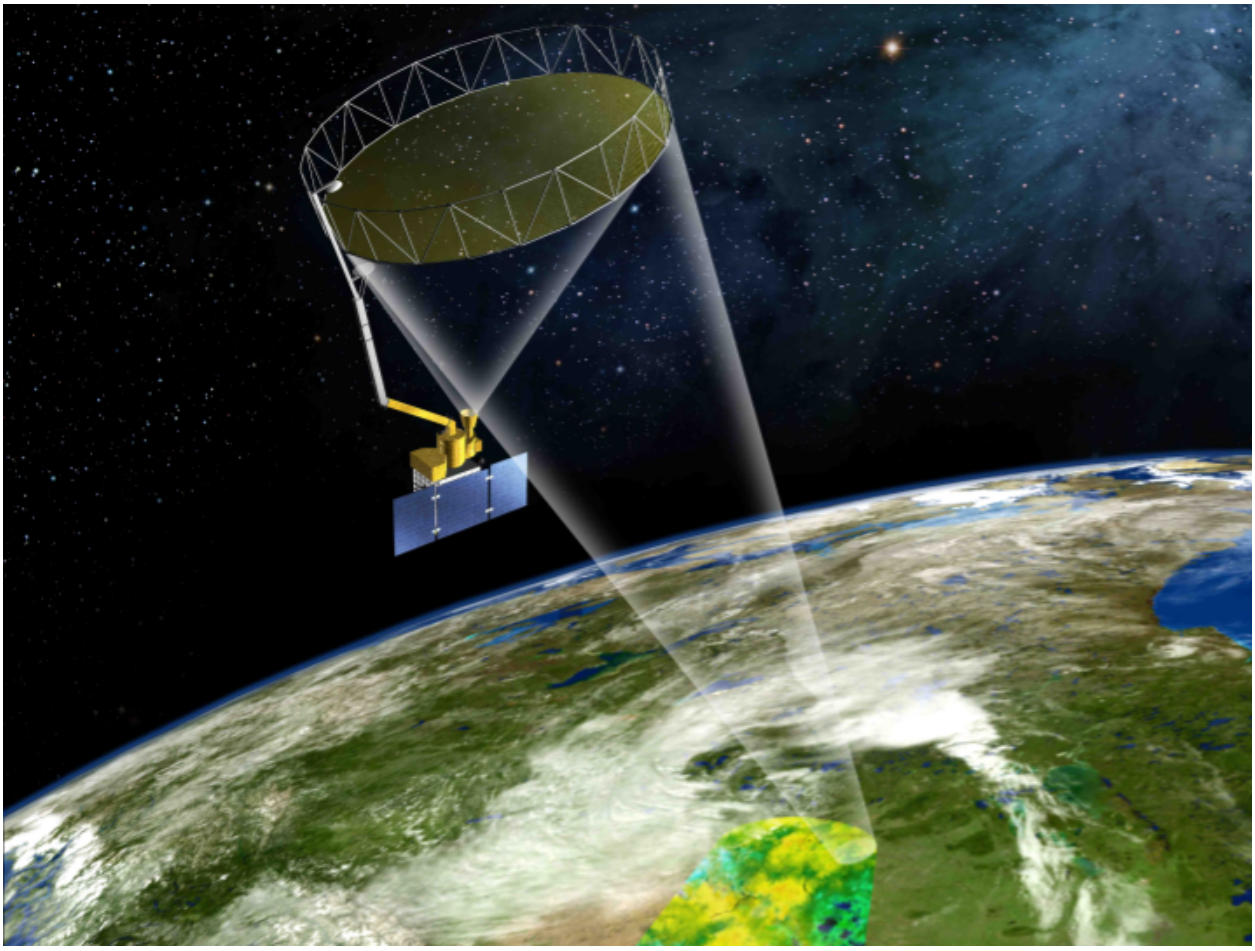

Figure 2.3: An artist's rendition of the SMAP spacecraft in orbit. The different colored portion of the Earth's surface represents the measurement swath that is generated by rotating the antenna as the spacecraft moves through its orbit.

receive windows of 4 pulse repetition intervals (PRIs) of the radar (see Fig. 2.5). During this time, the antenna rotates which slightly stretches the footprint on the ground. Each packet contains the integrated measurement for the full bandwidth as well as for 16 subbands. The subbands are used to help detect and mitigate the effects of radio frequency interference (RFI). If only one or a few subbands are affected by RFI they can just be thrown out and the measurment can still be taken with the other subbands.

The radar can be operated as a real aperture radar or as a SAR. The former is used to minimize the amount of data needed to be downlinked. The SAR mode is used only over land where it is combined with the radiometer measurements to estimate soil moisture at higher resolution. In either mode, the radar operates with a tunable center frequency

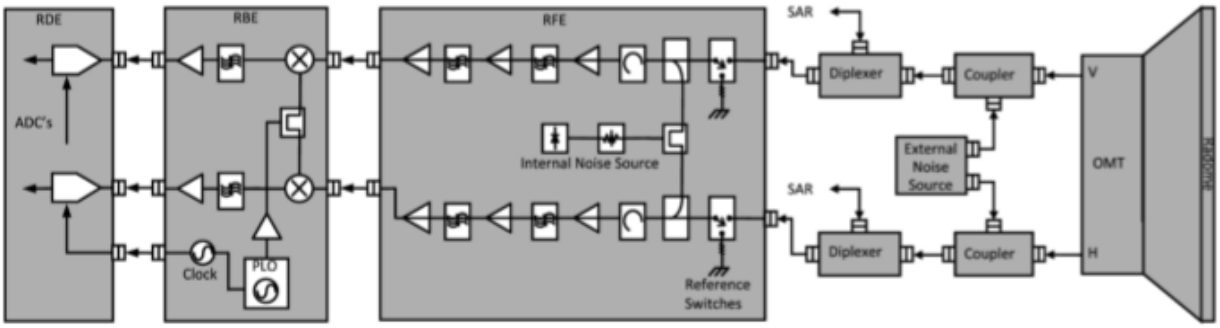

Figure 2.4: Block diagram of SMAP radiometer components. Taken from [3].

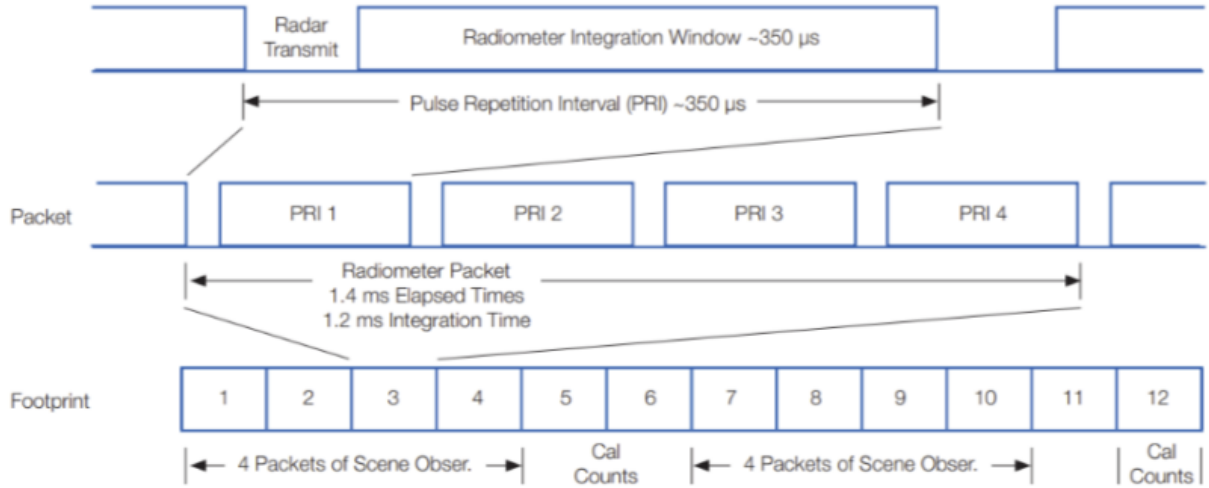

Figure 2.5: Timing of SMAP radiometer measurements. Taken from [6].

between 1217.25 and 1275.75 MHz. The vertical polarization transmit pulse and receive filter are cenetered 1.5 MHz below the center frequency, while the horizontal polarization transmit pulse and receive filter are centered 1.5 MHz above the center frequency. Both of the filters, in addition to a noise-only filter at the center frequency have a bandwidth of 1 MHz (see Fig. 2.6). The radar has a pulse repetition frequency (PRF) of approximately 2.9 kHz which corresponds to a PRI of 350 μs. Each transmit pulse is 15 μs, and due to the long time of flight from the spacecraft to the Earth and back the echo returns after 16 other pulses have been transmitted. The echos are stretched in time because the distances to the front and back of the footprints are significantly different. The radar has a peak transmit power of 500 W.

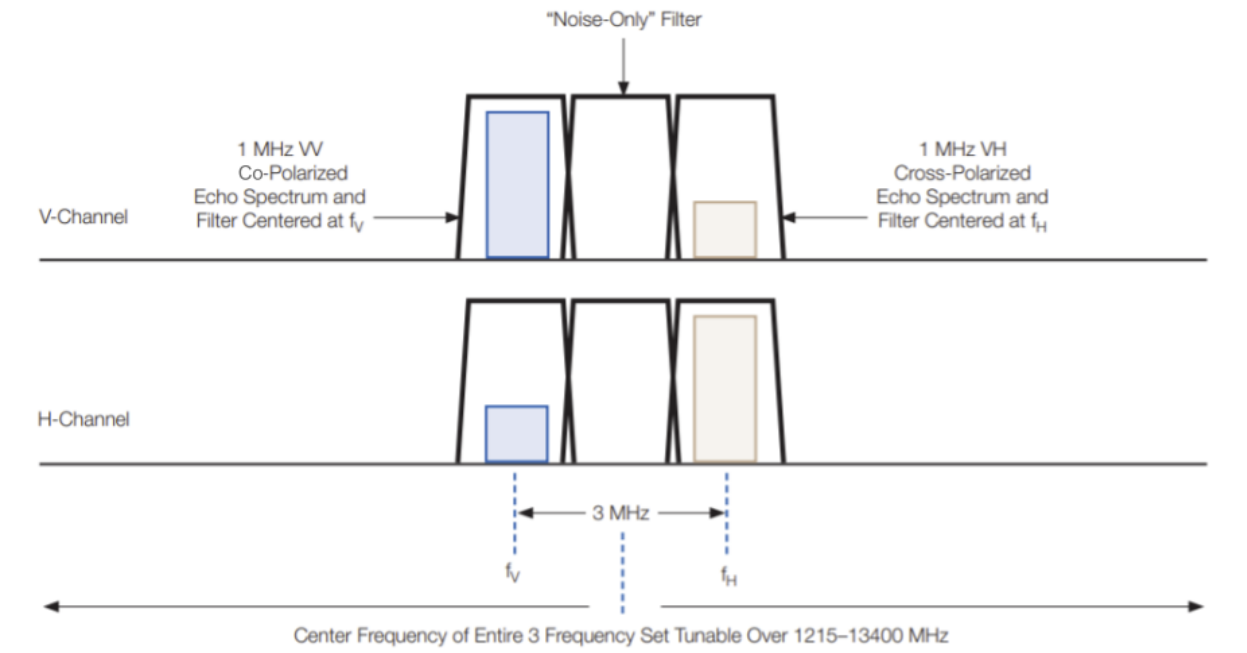

Figure 2.6: Frequencies of SMAP radar. Taken from [6].

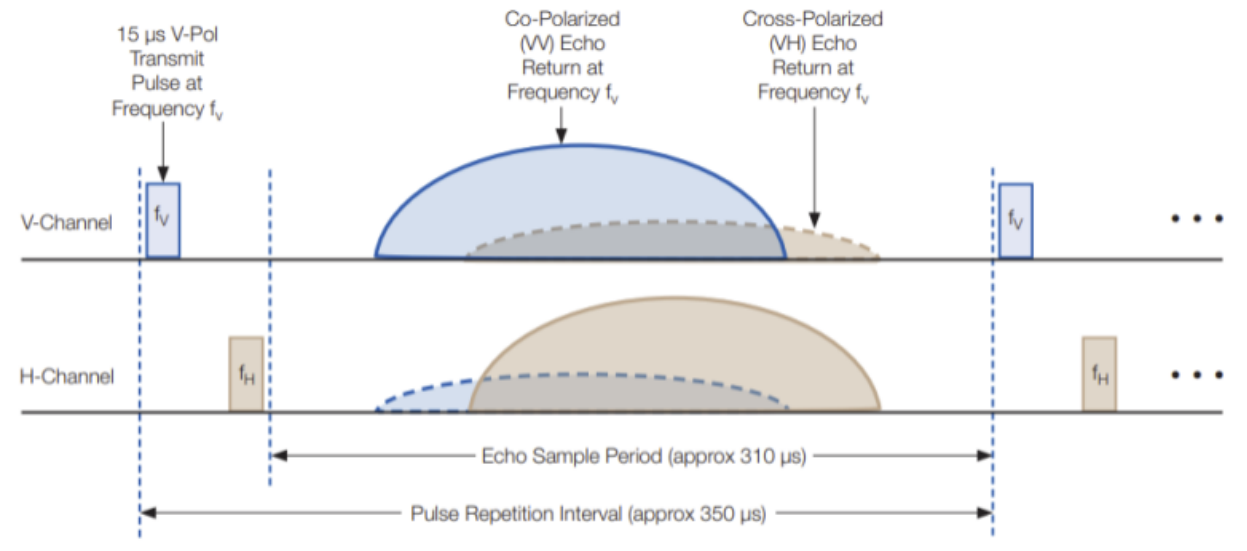

Figure 2.7: Timing of SMAP radar measurements. Taken from [6].

The GLOWS mission will replicate this design with only a few differences. As part of the development of the unified framework for GLOWS, Chapter 4 describes the validation of the translation of the measurement requirements to instrument requirements. This validation ensures that using similar instrument design parameters enables GLOWS to meet the same measurement requirements as SMAP. The effects of the change in antenna are analyzed in detail in Chapter 5.

CHAPTER 3. UNIFIED GEOMETRY FRAMEWORK

The first step in creating a unified framework for modeling and evaluating the GLOWS mission is creating a unified framework for all necessary geometry calculations. Modeling remote sensing observations from space requires precise geometry because even a small angle difference over the several hundred kilometers between the satellite and the surface can correspond to a large difference in location on the surface of the Earth. The MERS lab has several different geometry packages which have been developed over several decades. These functions and packages were combined and used as the basis for creating a new, unified package in MATLAB and Python. The algorithms used in several functions were also improved to be more accurate and/or run faster. This chapter contains the documentation for all of the geometry functions adapted from [7].

3.1 Important Background

This section describes several important background topics before they are used in the calculations of various geometric quantities later in the chapter. The topics include the effects of the Earth not being a perfect sphere on the geometry, the various reference frames involved, and methods for converting between reference frames.

3.1.1 Effects of the Earth's Oblateness

Due to its rotation, the Earth is oblate, which means that it is actually an ellipsoid, not a perfect sphere. The radius from the center of the Earth to the poles is about 10 kilometers less than the radius from the center of the Earth to the equator. This complicates several of the calculations.

Equations of Ellipses and Ellipsoids

In order to model the Earth as an ellipsoid, one must utilize the equations for ellipses and ellipsoids. An ellipse centered at the origin can be represented by two different equations:

$$\frac{x^2}{A^2} + \frac{y^2}{B^2} = 1 \tag{3.1}$$

or the parametric equations

$$x = A\cos t \tag{3.2}$$

$$y = B\sin t, \tag{3.3}$$

where A is the radius along the x axis and B is the radius along the y axis in both cases, and t is the arbitrary parameter of the parametric equations.

The parameter t can be easily confused with the geocentric latitude (described in Section 3.1.1). In the case of a circle, these two angles are the same, but in the case of an ellipse, they are not. This can be proven by considering the calculation of the geocentric latitude of a point on the surface of the ellipse. The tangent of the geocentric latitude ϕ is defined as

$$\tan\phi = \frac{B\sin t}{A\cos t}, \tag{3.4}$$

where $B\sin t$ is the y component of the position and $A\cos t$ is the x component. That relationship can be simplified to

$$\tan\phi = \frac{B}{A}\tan t, \tag{3.5}$$

which shows that the tangents of the geocentric latitude and the parametric variable are related by the ratio of the radii of the ellipse.

An ellipsoid is similarly defined by the equation

$$\frac{x^2}{A^2} + \frac{y^2}{B^2} + \frac{z^2}{C^2} = 1, \tag{3.6}$$

where A, B, and C are the radii along the axis which they divide in the equation. In the case of the Earth ellipsoid, A and B are equal so C is often omitted and the equation is instead

written as

$$\frac{x^2}{A^2} + \frac{y^2}{A^2} + \frac{z^2}{B^2} = 1, \tag{3.7}$$

where A is the equatorial radius of the Earth and B is the polar radius. The WGS84 definition of the reference ellipsoid for the Earth defines the equatorial radius to be 6,378,137.0 m and the polar radius to be 6,356,752.314245 m.

Identifying Positions on the Earth's Surface

One aspect affected by the oblateness of the Earth is the identification of any point on its surface. The general way to identify a position is by its latitude and longitude. For a sphere, this is a straightforward process with no complications, but for an ellipsoid there are complications in the definition of latitude as defined below.

Longitude is defined as the angle between the 0 degrees longitude axis (the prime meridian) and the projection of a position vector onto the equatorial plane (See Fig. 3.1). Longitude can be reported from $-180°$ to $180°$ with negative corresponding with West and positive corresponding with East or from $0°$ to $360°$.

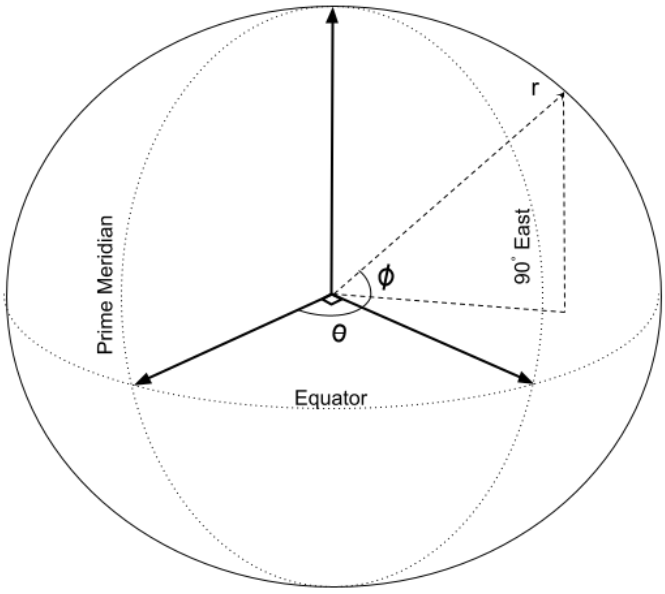

Figure 3.1: Illustration of geocentric latitude ϕ and longitude θ.

Latitude can be defined in one of two ways: geocentric or geodetic. Geocentric latitude is the angle made between a line from a point to the center of the earth and the equatorial plane. Geodetic latitude is the angle made between a line normal to the Earth's surface and the equatorial plane. Figure 3.2a illustrates this principle.

Nadir Point

The ellipsoidal nature of the Earth also affects the definition of the up and down direction at any point on or around the Earth. The point directly below a spacecraft is called its nadir point and is defined as the point on the surface of the ellipsoid closest to the spacecraft, which is also where a line between the spacecraft and the Earth's surface is normal to the surface (Fig. 3.2b). In order to maintain a consistent angle in how the instrument is viewing the Earth, a spacecraft's attitude must be constantly adjusted to be pointing at the nadir point.

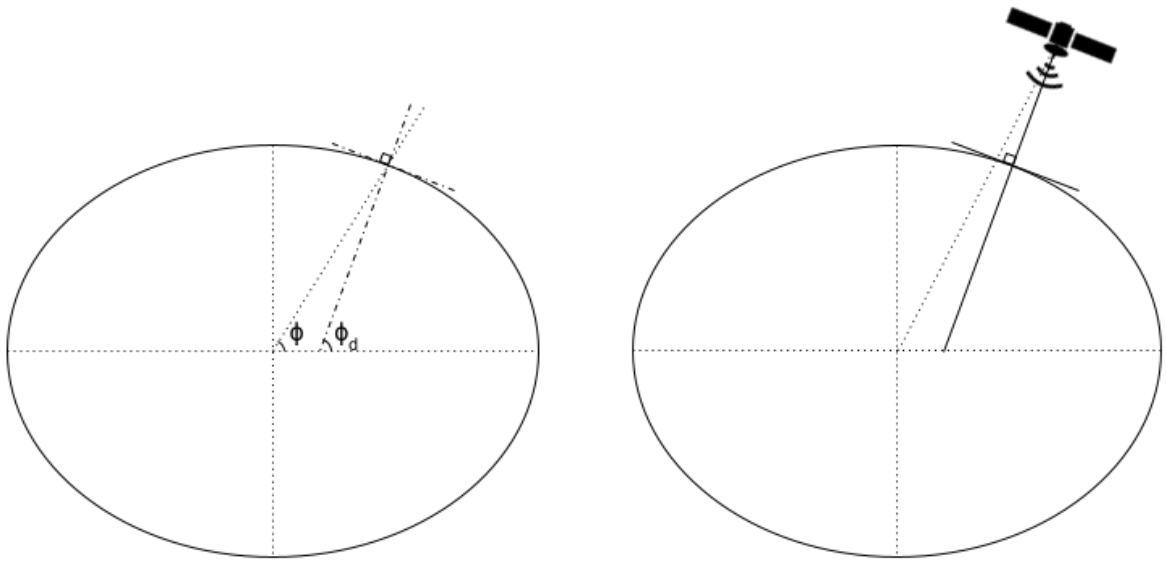

(a) (b)

Figure 3.2: Illustration of geocentric and geodetic geometry. (a) ϕ is the geocentric latitude of the point on the surface of the ellipsoid. ϕ_d is the geodetic latitude of the same point. (b) The dashed line represents the geocentric position vector of the spacecraft. The solid line represents the nadir direction from the spacecraft.

3.1.2 Reference Frames

Another complication in the geometry algorithms is that positions and directions can be defined as vectors in several different reference frames. This section defines each of the reference frames used between the spacecraft and the Earth. All frames are right-hand frames (the cross product of the x-axis vector and the y-axis vector is the z-axis vector).

Earth-Centered, Earth-Fixed (ECEF) Frame - (I,J,K)

The Earth-Centered, Earth-Fixed reference frame is the standard reference frame in which all of the geometric calculations are performed. The frame is defined as follows (see Figure 3.3):

- I (the x-axis) points at the intersection of the Prime Meridian and the Equator
- J (the y-axis) points at 90 degrees longitude
- K (the z-axis) points at the geographic north pole

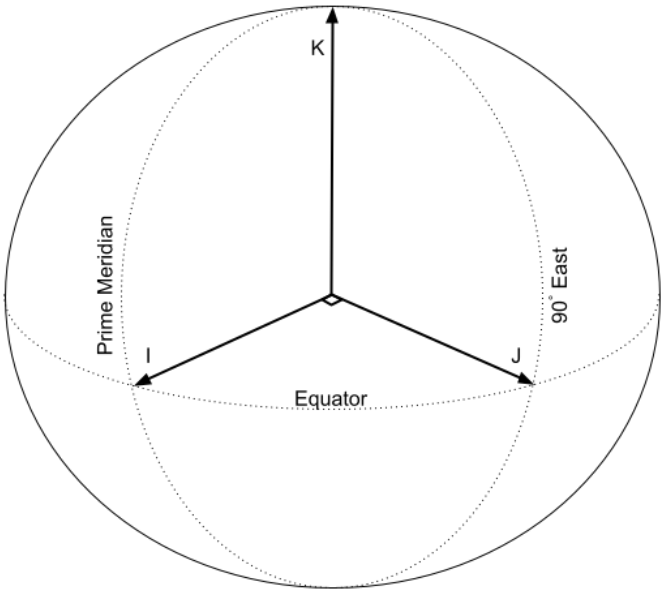

Figure 3.3: Illustration of the Earth-Centered Earth Fixed reference frame.

Geocentric Orbital Frame - ($\mathbf{u}_o$,$\mathbf{v}_o$,$\mathbf{w}_o$)

The geocentric orbital frame is centered at the spacecraft and pointed at the center of the Earth (see Figure 3.4a).

- u_o (the x-axis) points generally in the direction of the velocity, is in the orbital plane, and is the cross product of v_o and w_o
- v_o (the y-axis) points in the negative direction of the orbital angular momentum vector, which means it is normal to the orbital plane
- w_o (the z-axis) points from the spacecraft to the center of the earth, is in the orbital plane, and is the negative of the position vector in ECEF

Geodetic/Nadir Orbital Frame - ($\mathbf{u}_n$,$\mathbf{v}_n$,$\mathbf{w}_n$)

The geodetic or nadir orbital frame is centered at the spacecraft and pointed at the nadir point on the Earth's surface. All axes from the geocentric orbital frame are rotated such that the w_n axis is pointed at the nadir point (see Figure 3.4b). Because the nadir point only differs from the intersection of the geocentric vector with the surface in latitude, the w_n vector may not be in the orbital plane. Rotating all axes to align with nadir therefore generally removes any physical meaning from the other axes.

Spacecraft-Fixed Frame - ($\mathbf{x}_s$,$\mathbf{y}_s$,$\mathbf{z}_s$)

The spacecraft-fixed frame is a frame centered at the center of mass of the spacecraft and defined relative to the structure of the spacecraft. This frame is completely arbitrary, but generally is defined in such a way that makes observations simple, such as the z direction being the direction that needs to point at nadir. An example frame can be seen in Figure 3.5a. The orientation of the spacecraft-fixed frame is dependent on the attitude of the spacecraft. The attitude is measured by three rotations: roll, pitch, and yaw about the (u_n,v_n,w_n) axes, respectively.

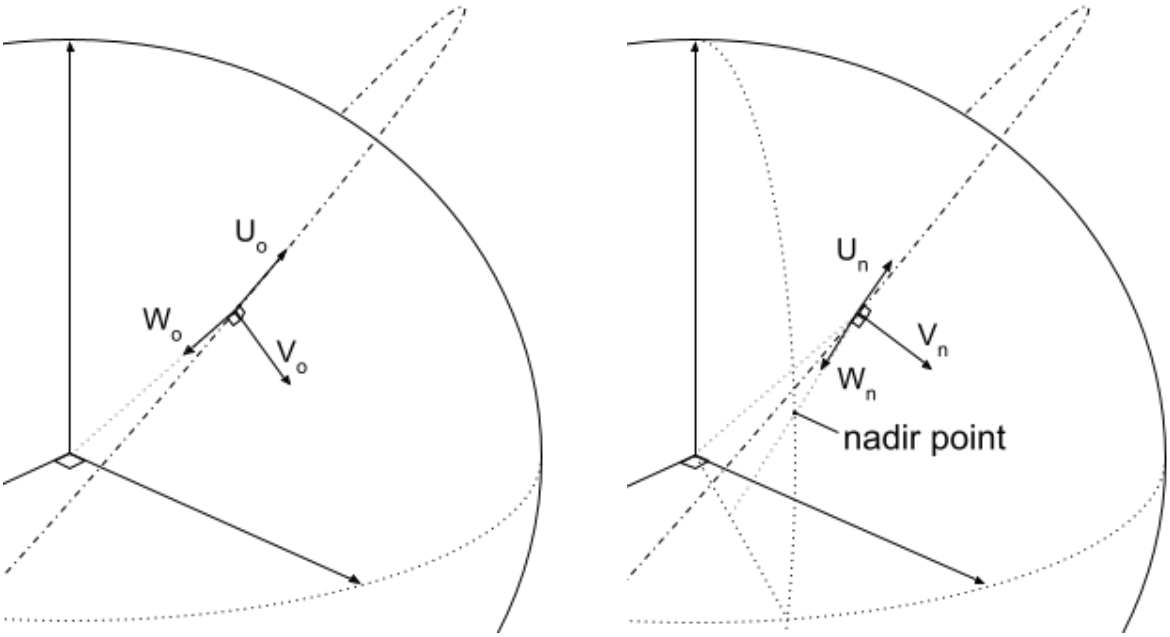

(a) (b)

Figure 3.4: (a) Illustration of the geocentric orbital frame. (b) Illustration of the geodetic orbital frame. The difference between the nadir point and the intersection of the geocentric position vector and the Earth's surface has been exaggerated to help visualize the difference between the geocentric and geodetic orbital frames.

Antenna-Fixed Frame - (x_a,y_a,z_a)

The antenna-fixed frame is centered at the antenna and defined relative to its structure, just like the spacecraft fixed frame. An example frame can be seen in Figure 3.5b. The distance between the centers of the spacecraft- and antenna-fixed frames can generally be disregarded in calculations since it is several orders of magnitude smaller than the distance between the spacecraft and the surface of the Earth. The orientation of the antenna-fixed frame is dependent on the attitude of the antenna (many antennas on remote sensing spacecraft rotate) which is also measured by three rotations: roll, dip, and azimuth about the (x_s,y_s,z_s) axes, respectively. The difference in naming between these attitude rotations and the spacecraft's attitude rotations is just to distinguish them from each other more easily.

Then antenna-fixed frame is generally defined such that the x-axis is pointing in the boresite direction of the antenna. This means that the axes need to be swapped in addition to rotating the spacecraft-fixed frame.

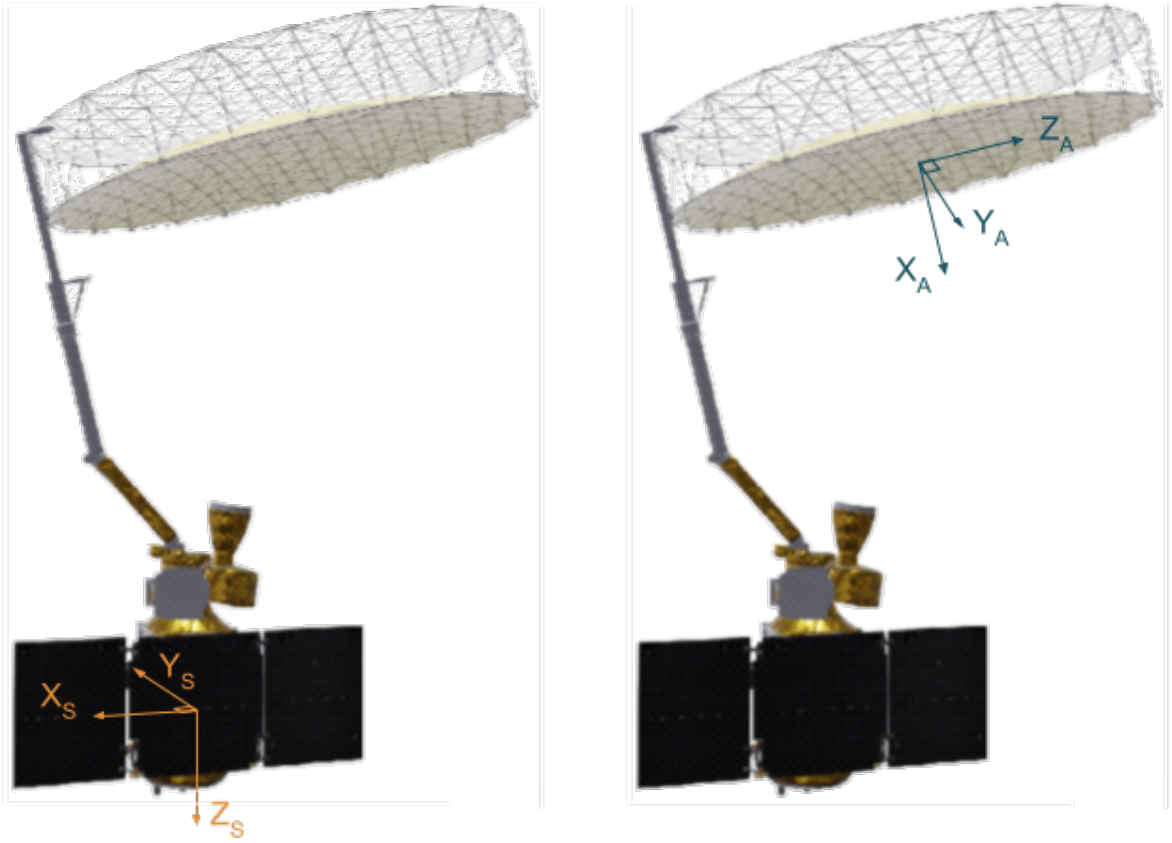

(a) (b)

Figure 3.5: (a) Illustration of an example spacecraft-fixed frame. (b) Illustration of an example (possibly rotating) antenna-fixed frame. The Soil Moisture Active Passive (SMAP) spacecraft is used as the spacecraft model.

Geographic North, East, Down Frame (NED) - (N,E,D)

The geographic North, East, Down Frame is centered at a point on the surface of the Earth and orients vectors relative to the geography at that point. This frame is used to determine the orientation of vectors to be able to calculate things like incidence angles, and azimuth angles relative to North.

- N (the x-axis) points North, is parallel to lines of longitude
- E (the y-axis) points East, is parallel to lines of latitude
- D (the z-axis) is a unit vector pointing from the location on the Earth's surface toward the middle of the Earth along the normal vector at that point

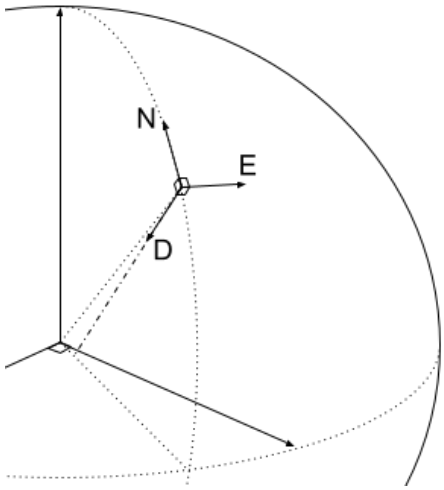

Figure 3.6: Illustration of the geographic North, East, Down reference frame.

3.1.3 General Methods for Conversion Between Frames

In order to perform all of the calculations in the ECEF frame, vectors in other frames need to be converted to that one. Several equivalent methods of converting between frames are explained in this section. The details of conversion between specific frames are discussed in the implementation section.

Rotation Around Standard Axes

The most general conversion between frames is a set of rotations around each of the axes (e.g., roll, pitch, and yaw). This is the simplest conversion method if the angles of rotation around each axis are already known. Rotation matrices are defined to rotate a vector by θ radians around the axis indicated in the subscript.

$$R_x = \begin{bmatrix} 1 & 0 & 0 \\ 0 & \cos\theta & -\sin\theta \\ 0 & \sin\theta & \cos\theta \end{bmatrix} \tag{3.8}$$

$$R_y = \begin{bmatrix} \cos\theta & 0 & \sin\theta \\ 0 & 1 & 0 \\ -\sin\theta & 0 & \cos\theta \end{bmatrix} \tag{3.9}$$

$$R_z = \begin{bmatrix} \cos\theta & -\sin\theta & 0 \\ \sin\theta & \cos\theta & 0 \\ 0 & 0 & 1 \end{bmatrix} \tag{3.10}$$

It is important to note that the multiplication of rotation matrices is not commutative. This means that rotations must all be done in the exact order in which they were measured. The same rotations applied in different orders can yield very different results.

Rotation About an Arbitrary Axis

One way to avoid the confusion of rotation orders is to rotate around a single arbitrary axis. The result is the same as the combination of the three rotations, but there is no need to know the three angles. This is the simplest way to determine the rotation needed to align one known vector with another. If the two vectors are corresponding axes from different frames, then the rotation between the two vectors is the same rotation required to convert any vector between the frames.

The process of rotation about an arbitrary axis is well defined in several resources, one of which is included with this documentation for those interested. The definition of the rotation matrix is the following [8]:

$$R = \begin{bmatrix} tu_x^2 + C & tu_xu_y - Su_z & tu_xu_z + Su_y \\ tu_xu_y + Su_z & tu_y^2 + C & tu_yu_z - Su_x \\ tu_xu_z - Su_y & tu_yu_z + Su_x & tu_z^2 + C \end{bmatrix}, \tag{3.11}$$

where $\vec{r} = (u_x, u_y, u_z)$ is the unit vector of the axis around which to rotate, θ is the angle by which to rotate around the axis, $C = \cos\theta$, $S = \sin\theta$, and $t = 1 - \cos\theta$.

Orthonormal Bases and Change of Basis

An orthonormal basis is a set of orthogonal and normal (unit) vectors that spans a vector space. Orthonormal bases are the foundation of coordinate systems. A coordinate set is just a representation of a linear combination of the orthonormal basis vectors that define

the reference frame. Within a reference frame, the orthonormal basis vectors are defined to be {(1,0,...,0),(0,1,...,0),...,(0,0,...,1)} with the size and number of vectors depending on the dimension of the space. If the basis vectors can be defined in another frame, performing a change of basis to the other frame is trivial, it just requires multiplying the vector in the original frame by the basis vectors defined in the new frame. The matrix composed of the transformed orthonormal basis vectors is equal to the result of multiple rotation matrices, but is easier to calculate in instances where the angles of rotation are not known, but vectors in the direction of the axes are.

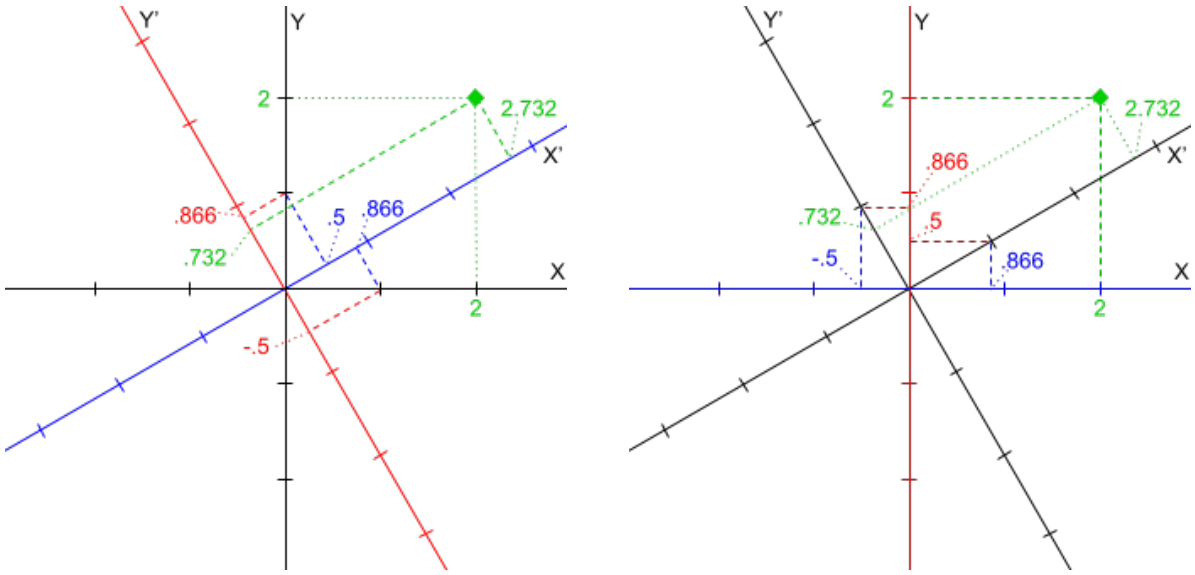

Figure 3.7: Change of basis example. In both (a) and (b), the green point is being changed from the basis defining the black axes to the basis defining the blue and red axes. The dashed green lines show the components of the vector in the basis being converted too, while the dotted green lines show the components in the basis being converted from. The red and blue dashed lines show the x (blue) and y (red) components of the basis vectors in the current basis in the basis to be converted to. These values are used to construct the change of basis matrices. (a) converting from the X,Y basis to the X',Y' basis. (b) converting from the X',Y' to the X,Y basis.

The following example illustrates this concept in two dimensions where a new X',Y' frame is defined as a 30 degree counterclockwise rotation of the standard cartesian X,Y frame. Fig. 3.7 visualizes the components of a coordinate to convert in two different bases

as well as the components of the basis vectors in the other basis. To convert from one frame to the other, one can simply create a matrix composed of the column vectors of the orthonormal basis vectors of one frame defined in the other frame's coordinates. For example the conversion matrix to change basis in Fig. 3.7a from X and Y to X' and Y' is:

$$R_1 = \begin{bmatrix} 0.866 & 0.5 \\ -0.5 & 0.866 \end{bmatrix}. \tag{3.12}$$

The first column is the (1,0) vector in the X,Y frame, which has components (0.866, -0.5) in the X',Y' frame, and the second column is the (0,1) vector in the X,Y frame, which has components (0.5,0.866) in the X',Y' frame. To change basis from the X,Y basis to the X',Y' basis, multiply the vector in the X,Y basis by R_1:

$$\begin{bmatrix} 0.866 & 0.5 \\ -0.5 & 0.866 \end{bmatrix} \begin{bmatrix} 2 \\ 2 \end{bmatrix} = \begin{bmatrix} 2.732 \\ 0.732 \end{bmatrix}. \tag{3.13}$$

The resultant vector exactly matches what the expected components of the coordinate in the X',Y' frame are as labeled in the figure.

The same can be done to change from the X',Y' frame to the X,Y frame as illustrated in Fig. 3.7b. The matrix of the components of the unit vectors in the X',Y' frame defined in the X,Y frame is:

$$R_2 = \begin{bmatrix} 0.866 & -0.5 \\ 0.5 & 0.866 \end{bmatrix}. \tag{3.14}$$

Multiplying the coordinates in the X',Y' frame by that matrix yields:

$$\begin{bmatrix} 0.866 & -0.5 \\ 0.5 & 0.866 \end{bmatrix} \begin{bmatrix} 2.732 \\ 0.732 \end{bmatrix} = \begin{bmatrix} 2 \\ 2 \end{bmatrix}. \tag{3.15}$$

This result matches the vector components in the X,Y frame.

Note that R_2 is simply R_1^T. This relationship is true for any pair of orthonormal bases. If the orthonormal basis vectors of one frame can be defined in the other frame, the

matrix of those vectors can be used to convert between both frames. The matrix just needs to be transposed when converting in the opposite direction of the definition of the vectors.

In the simple two-dimensional example described, it probably would be easier just to create the rotation matrix (especially because the sine and cosine calculations were necessary in defining the basis vectors in the other frames anyway), but if it is easier to define the basis vectors than figure out rotation angles, then creating the change of basis matrix can be much simpler.

3.2 Theory of Calculations

Utilizing the theory in the background section as well as other fundamental concepts from geometry and linear algebra, the various algorithms to calculate the geometric parameters are constructed. Each algorithm's theoretical implementation is discussed in this section. The actual implementation in various programming languages may vary, but should all be based on the theory in this section.

3.2.1 Specific Implementation of Conversion Between Frames

The first functions to be covered are the conversion functions. These are prerequisite to all of the other functions since all vectors need to be in the ECEF frame in order to calculate the geometric parameters.

Antenna-Fixed to Spacecraft-Fixed

As mentioned in the background, the antenna-fixed frame is defined as a rotation of the spacecraft-fixed frame by the attitude of the spacecraft which is measured as three rotations: roll, dip, and azimuth about the $\vec{x_s}$, $\vec{y_s}$, and $\vec{z_s}$ axes, respectively. Because the three rotations are known, multiplication by the three rotation matrices is the simplest conversion method. It is crucial that these are done in the same order that the measurements are defined in, however. In this software, the order is defined as roll, then pitch, then yaw, meaning that

the conversion matrix C_{ant}^{sc} is defined as

$$C_{ant}^{sc} = R_{azimuth} R_{dip} R_{roll}. \tag{3.16}$$

If the antenna's attitude measurements follow a different order, then either the measurements or the conversion function must be modified. The columns of C_{ant}^{sc} must also then be rearranged because the x and z axes of the antenna- and spacecraft-fixed frames are swapped and the y-axis is negated between the two. The first and third columns get swapped and the second column is negated.

Spacecraft-Fixed to Nadir Orbital

As mentioned in the background, the spacecraft-fixed frame is defined as a rotation of the nadir orbital frame by the attitude of the spacecraft which is measured as three rotations: roll, pitch, and yaw about the $\vec{u_o}$, $\vec{v_o}$, and $\vec{w_o}$ axes, respectively. Because the three rotations are known, multiplication by the three rotation matrices is the simplest conversion method. It is crucial that these are done in the same order that the measurements are defined in, however. In this software, the order is defined as roll, then pitch, then yaw, meaning that the conversion matrix C_{sc}^{nadir} is defined as

$$C_{sc}^{nadir} = R_{yaw} R_{pitch} R_{roll}. \tag{3.17}$$

If the spacecraft's attitude measurements follow a different order, then either the measurements or the conversion function must be modified.

Nadir Orbital to Geocentric Orbital

Because the $\vec{w_o}$ and $\vec{w_n}$ vectors can easily be defined, this conversion is implemented using rotation about an arbitrary axis. $\vec{w_o}$ is just the normalized negative of the spacecraft position vector. $\vec{w_n}$ is calculated by calculating the nadir position vector in ECEF (see Section 3.2.2) and normalizing the difference between the nadir position vector and the spacecraft position vector. Both of these vectors are currently defined in the ECEF frame,

but the conversion is defined in the orbital frames, so both vectors need to be converted to the geocentric orbital frame by multiplying by the matrix defined in section 3.2.1.

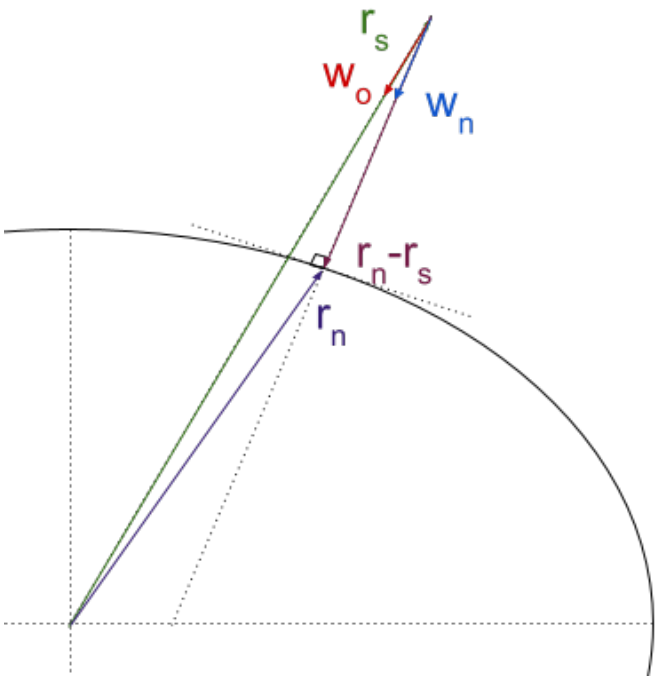

Figure 3.8: Illustration of the vectors involved in the conversion between geocentric and nadir orbital frames. The $\vec{w_o}$, $\vec{w_n}$, and $\vec{r_s} - \vec{r_n}$ vectors are drawn from $\vec{r_s}$ to visualize the relationship better.

To convert from the nadir to the geocentric orbital frame, then, is just a matter of rotating the same amount and about the same axis necessary to align $\vec{w_o}$ and $\vec{w_n}$. Then, the rotation about an arbitrary axis rotation matrix is constructed using the following: $\vec{r}$is the normalized cross product of $\vec{w_o}$ and $\vec{w_n}$, $\cos\theta$ is the dot product of $\vec{w_o}$ and $\vec{w_n}$, and $\sin\theta$ is the magnitude of the cross product. We can use the definitions of sin and cos since $\vec{w_o}$ and $\vec{w_n}$ are unit vectors. The resulting matrix converts nadir to geocentric orbital, and its transpose converts geocentric to nadir orbital.

Geocentric Orbital to ECEF

Converting from geocentric orbital to ECEF is most easily accomplished by change of basis because it is easy to compute the orthonormal basis vectors for the geocentric orbital

frame in the ECEF frame. $\vec{w_o}$ is the normalized negative spacecraft position vector (pointing from the spacecraft to the center of the Earth), $\vec{v_o}$ is the normalized cross product of $\vec{w_o}$ and the spacecraft velocity (normal to the orbital plane and the negative of the rotational momentum), and $\vec{u_o}$ is the normalized cross product of $\vec{v_o}$ and $\vec{w_o}$ (approximately in the direction of velocity for circular orbits, but not elliptical ones). Put the three vectors into a matrix, and that matrix can be used to convert any vector in the geocentric orbital frame to the ECEF frame. The transpose converts in the other direction.

ECEF to NED

The conversion from ECEF to NED also is most easily accomplished by change of basis, as the north, east, and down unit vectors can be defined easily given either the latitude and longitude of a point, or the up vector from which the latitude and longitude can be calculated. The components of each of the vectors are illustrated in Figure 3.9. Joining these vectors into a change of basis matrix yields:

$$C_{ECEF}^{NED} = \begin{bmatrix} -\cos\theta\sin\phi & -\sin\theta & -\cos\theta\cos\phi \\ -\sin\theta\sin\phi & \cos\theta & -\sin\theta\cos\phi \\ cos\phi & 0 & -sin\phi \end{bmatrix}, \tag{3.18}$$

where ϕ is the latitude and θ is the longitude.

3.2.2 Other Conversions

Geocentric Latitude to and From Geodetic Latitude

To define the conversion between geocentric and geodetic latitude, the geodetic latitude must first be defined. This is most easily accomplished by utilizing the parametric equations of the ellipse. The tangent vector at any point on the ellipse is defined as

$$\frac{d}{dt}\begin{bmatrix} A\cos t \\ B\sin t \end{bmatrix} = \begin{bmatrix} -A\sin t \\ B\cos t \end{bmatrix}. \tag{3.19}$$

Conversions.png Conversions.png

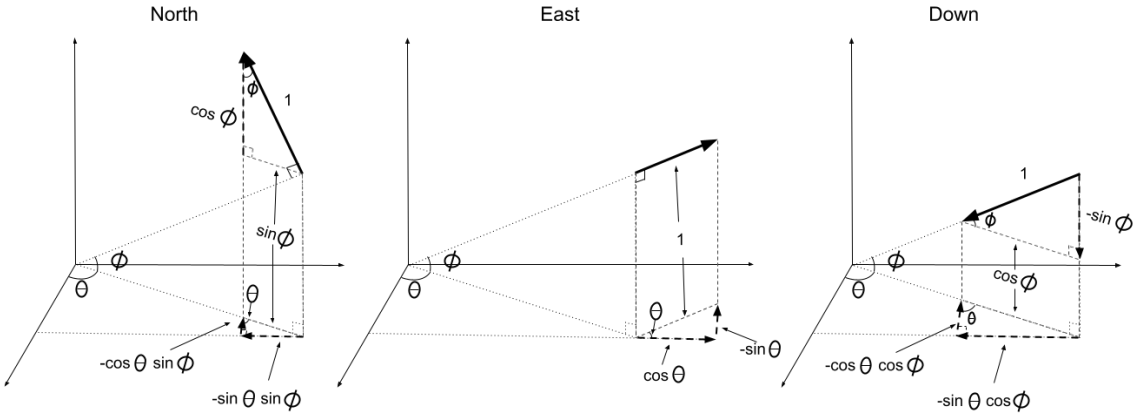

Figure 3.9: Illustration of the components of the basis vectors of the NED frame in the ECEF frame. These components are joined to make the conversion matrix between the two frames.

To find the normal vector to the tangent, simply rotate the tangent vector by -90 degrees which yields the vector $\begin{bmatrix} B\cos t \\ A\sin t \end{bmatrix}$. These vectors are illustrated in Fig. 3.10.

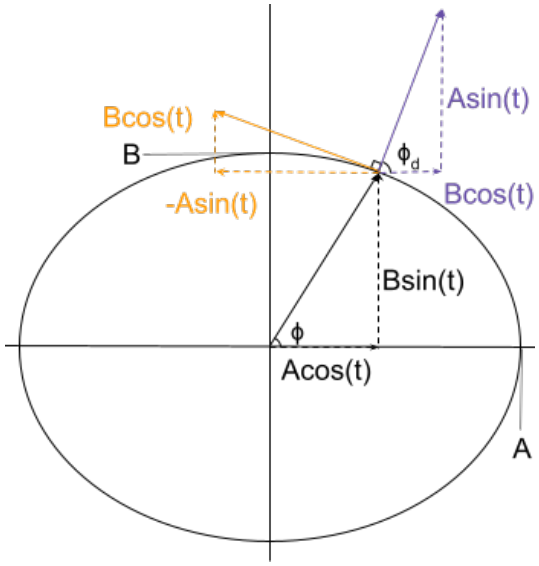

Figure 3.10: Illustration of the vectors involved in the relationship between geocentric and geodetic latitude. The black vector is the position vector of a point on the surface defined by the parameter t. The orange vector is the tangent vector to that point. The purple vector is the normal vector to that point. The geocentric latitude ϕ is determined from the black vector while the geodetic latitude ϕ_d is determined from the purple vector.

The tangent of the geodetic latitude ϕ_d can then be defined as

$$\tan\phi_d = \frac{A\sin t}{B\cos t}, \tag{3.20}$$

which can be simplified to

$$\tan\phi_d = \frac{A}{B}\tan t. \tag{3.21}$$

This relationship is not, however, a relationship between geodetic and geocentric latitudes, only between geodetic latitude and the parametric variable θ. In order to convert between the two latitudes, Eq. 3.5 must be rearranged and substituted into Eq. 3.21 yielding:

$$\tan\phi_d = \frac{A}{B}(\frac{A}{B}\tan\phi), \tag{3.22}$$

which can be further simplified to

$$\tan\phi_d = \frac{A^2}{B^2}\tan\phi. \tag{3.23}$$

This relationship is used to convert between the two types of latitude.

Geocentric (ECEF) to Geodetic Coordinates

The conversion from geocentric cartesian (x,y,z) coordinates in the ECEF frame to geodetic latitude, longitude, and height has been a topic of study for many years in the field of geodesy. Vermeille has published a closed-form algorithm for the conversion between the two sets of coordinates [9] which has been chosen as the basis for this conversion. This algorithm is likely not the most efficient, but is more efficient than the previous iterative algorithm used in the lab and more well documented. In the future, more research can be done to find a more efficient algorithm to replace Vermeille's if desired. His paper detailing the algorithm has been included with this documentation.

ECEF to and From Along- and Cross-Track Distance

The along- and cross-track distances of a point are defined as the distances from the nadir point of the spacecraft parallel and perpendicular to the direction of the spacecraft's velocity on the Earth's surface, respectively (see Fig. 3.11). These distances are calculated assuming the Earth is a sphere with the radius at the nadir latitude. This greatly simplifies the calculation and is adequate at the distances of typical remote sensing spacecraft swath widths, but does have some error.

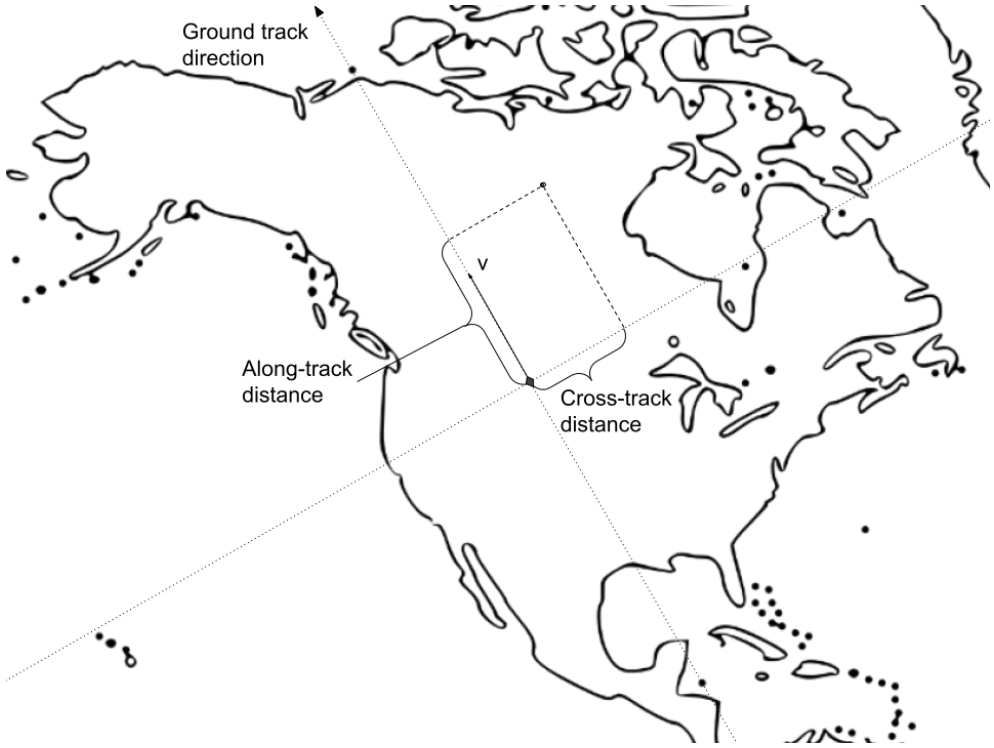

Figure 3.11: Illustration of the directions involved in along- and cross-track distances. The diamond at the origin of the dotted lines is the nadir point of a spacecraft. The vector $\vec{v}$ is the relative velocity of the spacecraft at the nadir point. The dot is the position for which the distances are being calculated. The dotted line parallel to the velocity vector is the along-track direction, and the dotted line perpendicular to the velocity vector is the cross-track direction.

The difference between a spherical distance and the geodesic (ellipsoidal) distance along a meridian at 45 degrees latitude where the error should be maximum is represented in Fig. 3.12. It is shown that the error is a quadratic function in the geodesic distance. For

instruments with smaller swaths (on the order of a few hundred km) that means the error is only a few hundred meters, but for swath widths over 1000 km, the error quickly approaches 1 km and more. This is another area where future research could be devoted. The concerns are that calculating the more accurate geodesic distances might be too complicated and inefficient.

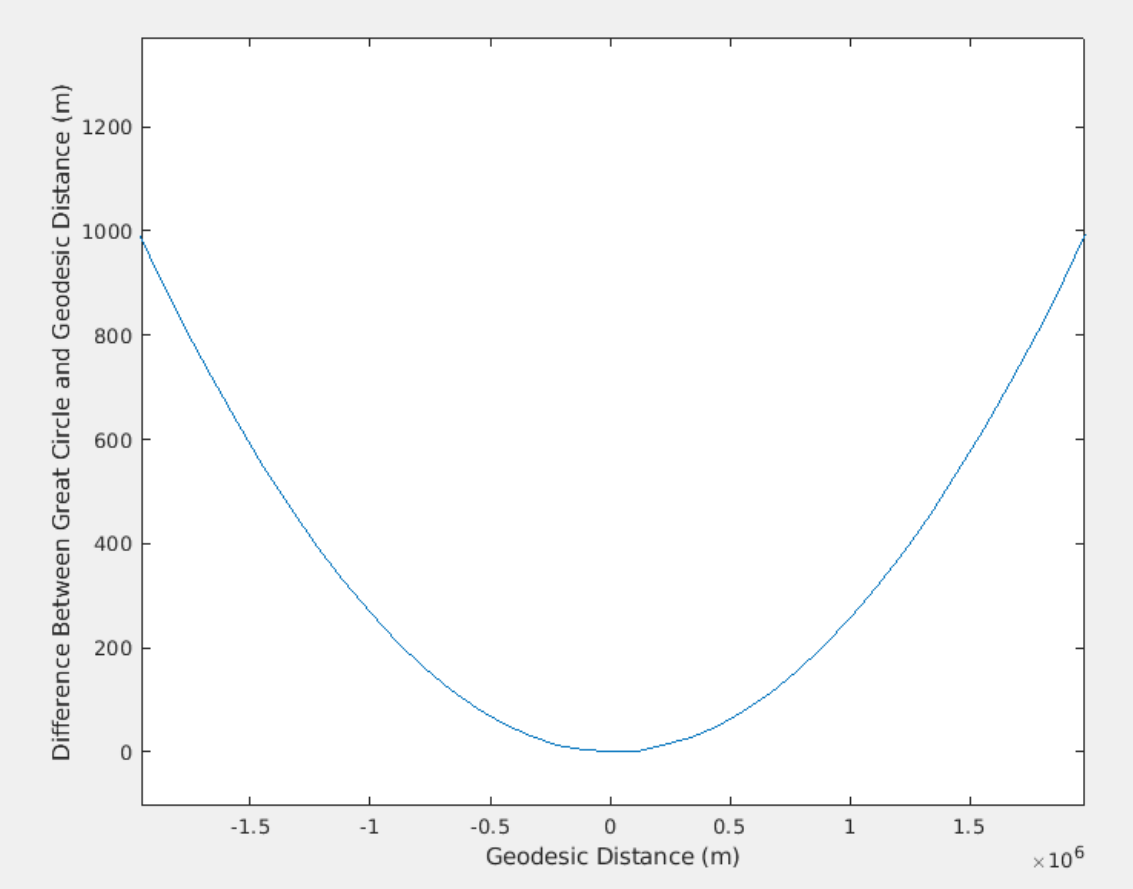

Figure 3.12: Plot of the error between great circle (spherical) and geodesic (ellipsoidal) distances along a meridian at 45 degrees latitude.

Calculating along- and cross-track distances with the assumption that the Earth is locally spherical is a calculation of arc lengths. An arc length is calculated as

$$d = r\alpha, \tag{3.24}$$

where d is the arc length, r is the radius, and α is the angle in radians of the arc. An arc length can be split into perpendicular components utilizing sines and cosines just like a hypotenuse of a right triangle. The total distance arc length is computed using Eq. 3.24 with r being the Earth's radius at the nadir point and alpha being the angle between the position vectors of the nadir point and the point on the surface for which the distances are being calculated. The along-track distance is then defined as

$$ad = d\cos\theta \tag{3.25}$$

and the cross-track distance is defined as

$$cd = d\sin\theta, \tag{3.26}$$

where θ is the difference in relative azimuth between the relative velocity vector at the nadir point and a vector from the nadir point to the other point.

3.2.3 Radius at Given Latitude

The radius at a given geodetic latitude is calculated utilizing the parametric equations for an ellipse. The geodetic latitude is first converted to the parametric variable θ using the relationship in Eq. 3.21. Then, the radius at the latitude can be calculated just by taking the magnitude of the vector with the components described by the parametric equations:

$$r_{lat} = \left\| \begin{bmatrix} A\cos\theta \\ B\sin\theta \end{bmatrix} \right\| \tag{3.27}$$

3.2.4 Earth Velocity at Surface Position

In order to calculate the relative velocity between the spacecraft and a point on the surface of the Earth, one must know the velocity of that point. The velocity of any point on the surface of the Earth is due to the Earth's rotation. Translating the Earth's rotational velocity into a linear velocity at a given point requires the rotational velocity vector and a

radial vector from the axis of rotation. The rotational velocity vector points perpendicular to the plane of rotation (which is the equatorial plane) following the right hand rule, so it points in the positive K direction in the ECEF frame. The entire magnitude of the rotational velocity is therefore in the K-axis component of the vector. The radial vector is created by taking the position vector and nulling the K-axis component. This leaves a vector with the radius from the axis of rotation, not from the center of the Earth, to the point. Calculating the linear velocity of the point is now just the cross product of the two vectors:

$$\vec{v_{surf}} = \vec{v_{rot}} \times \vec{r_{I,J}} \tag{3.28}$$

3.2.5 Pointing Vector Creation

Given the elevation angle θ and azimuth angle ϕ, a unit pointing vector in the antenna-fixed frame is created by rotating the unit vector pointing in the x direction about the y axis by the θ, then rotating the resultant vector about the z axis by ϕ. This is done to maintain consistency with elevation and azimuth as defined in an antenna gain pattern where both rotations are orthogonal to the boresight vector.

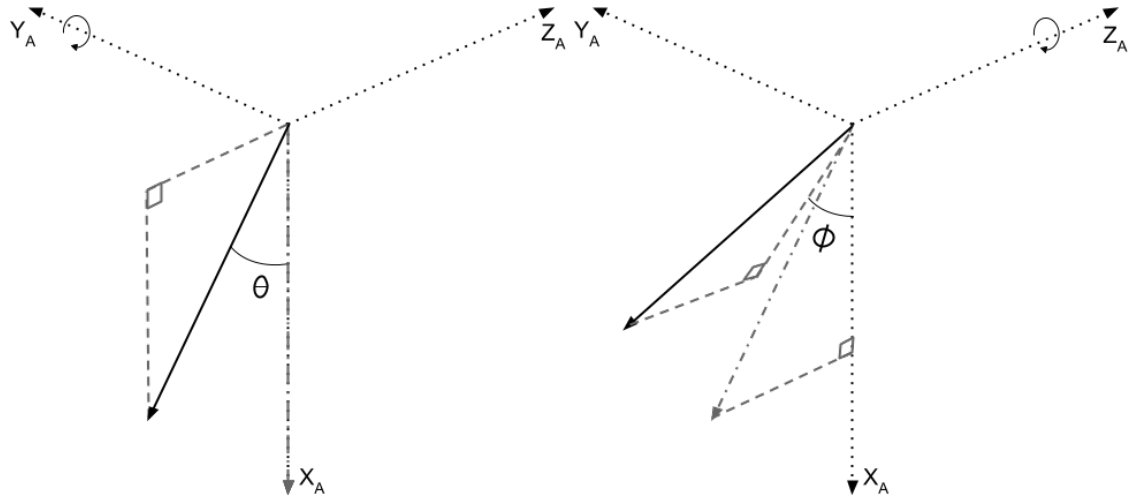

Figure 3.13: Illustration of the rotations involved in the creation of a pointing vector in the antenna-fixed frame.

These two rotations are represented by substituting the look angle into Eq. 3.9 and the azimuth angle into Eq. 3.10. Multiplying the original z-axis unit vector by these matrices yields

$$\vec{p} = \begin{bmatrix} \cos\phi & -\sin\phi & 0 \\ \sin\phi & -\cos\phi & 0 \\ 0 & 0 & 1 \end{bmatrix} \begin{bmatrix} -\cos\theta & 0 & \sin\theta \\ 0 & 1 & 0 \\ -\sin\theta & 0 & \cos\theta \end{bmatrix} \begin{bmatrix} 1 \\ 0 \\ 0 \end{bmatrix} \tag{3.29}$$

$$\vec{p} = \begin{bmatrix} \sin\theta\cos\phi \\ \sin\theta\sin\phi \\ \cos\phi \end{bmatrix} \tag{3.30}$$

3.2.6 Pointing Vector/Earth Surface Intersect Location

After a pointing vector from the antenna has been converted to the ECEF frame, the intersection of that vector with the surface of the Earth is determined using the equations defining a point on a line and a point on the surface on an ellipsoid. Any point $\vec{x}$ on a line defined by a vector $\vec{v}$ with an origin at $\vec{o}$ is just some multiple d of $\vec{v}$ from $\vec{o}$ as represented in the equation

$$\vec{x} = \vec{o} + d\vec{v}. \tag{3.31}$$

Any point $\vec{x}$ on the surface of an ellipsoid centered at the origin of the coordinate system is defined in terms of the radii a, b, and c along each axis as represented in the equation

$$\left\| \begin{bmatrix} \frac{1}{a} & 0 & 0 \\ 0 & \frac{1}{b} & 0 \\ 0 & 0 & \frac{1}{c} \end{bmatrix} \vec{x} \right\|^2 = 1. \tag{3.32}$$

In the case of the Earth, the equatorial radius r_e is equal on both the I and J axes, while the polar radius r_p along the K axis is shorter, so the equation for the Earth ellipsoid is

$$\left\| \begin{bmatrix} \frac{1}{r_e} & 0 & 0 \\ 0 & \frac{1}{r_e} & 0 \\ 0 & 0 & \frac{1}{r_p} \end{bmatrix} \vec{x} \right\|^2 = 1, \tag{3.33}$$

which, when multiplied by r_e^2, becomes

$$\left\| \begin{bmatrix} 1 & 0 & 0 \\ 0 & 1 & 0 \\ 0 & 0 & \frac{r_e}{r_p} \end{bmatrix} \vec{x} \right\|^2 = r_e^2. \tag{3.34}$$

Solving for the intersection point requires solving the system of equations formed by Eqs. 3.31 and 3.34. Substituting the value of $\vec{x}$ from Eq. 3.31 into Eq. 3.34 and letting $E = \begin{bmatrix} 1 & 0 & 0 \\ 0 & 1 & 0 \\ 0 & 0 & \frac{r_e}{r_p} \end{bmatrix}$ yields

$$\|E(\vec{o} + d\vec{v})\|^2 = r_e^2. \tag{3.35}$$

This is a quadratic equation with variable d, which can be expanded by evaluating the dot product

$$(E\vec{o} + dE\vec{v}) \cdot (E\vec{o} + dE\vec{v}) = r_e^2 \tag{3.36}$$

to

$$d^2(E\vec{v} \cdot E\vec{v}) + d(E\vec{o} \cdot E\vec{v}) + E\vec{o} \cdot E\vec{o} - r_e^2 = 0. \tag{3.37}$$

d can be found by solving the quadratic formula with

$$a = E\vec{v} \cdot E\vec{v} = v_I^2 + v_J^2 + \frac{r_e^2}{r_p^2} v_K^2 \tag{3.38}$$

$$b = E\vec{o} \cdot E\vec{v} = o_I v_I + o_I v_J + \frac{r_e^2}{r_p^2} o_k v_K \tag{3.39}$$

$$c = E\vec{o} \cdot E\vec{o} - r_e^2 = o_I^2 + o_J^2 + \frac{r_e^2}{r_p^2} o_K^2 - r_e^2. \tag{3.40}$$

If there are no real roots, then the vector never intersects the surface. Otherwise, the smaller of the two roots can be substituted back into d in Eq. 3.31 to find the ECEF coordinates of the intersection.

3.2.7 Slant Range

The slant range s is the distance between the antenna and the target. Given two vectors, the slant range is easily calculated as the magnitude of the difference between the two vectors:

$$s = \left\| \vec{r_{surf}} - \vec{r_s} \right\|, \tag{3.41}$$

where $\vec{r_{surf}}$ is the position vector of the target on the surface of the Earth and $\vec{r_s}$ is the position vector of the spacecraft (see Fig. 3.14).

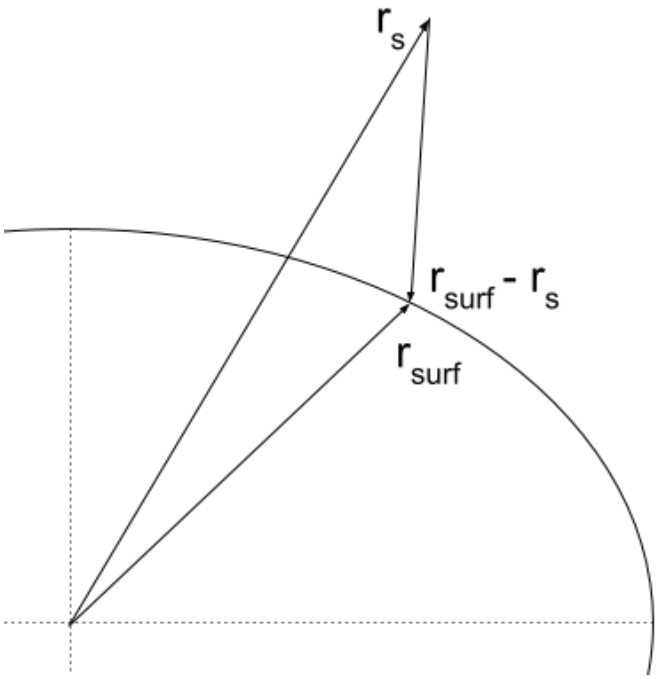

Figure 3.14: Illustration of vectors involved in slant range computation. $\vec{r_s}$ is the spacecraft position vector, $\vec{r_{surf}}$ is the surface point position vector, and the slant range is the magnitude of the difference between them.

3.2.8 Incidence Angle

The incidence angle θ_{inc} is the angle between the pointing vector from the instrument and the local vertical. The local vertical is determined by transforming the geocentric position vector of the point at which to calculate the incidence angle to a geodetic vector as follows:

$$\vec{r_{geodetic}} = \begin{bmatrix} \frac{r_I}{A^2} \\ \frac{r_J}{A^2} \\ \frac{r_K}{B^2} \end{bmatrix}, \tag{3.42}$$

where r_I, r_J, and r_K are the components of the geocentric position vector and A and B are the equatorial and polar radii of the Earth respectively. Both the pointing vector and the vertical vector are normalized and then the incidence angle is calculated as:

$$\theta_{inc} = \frac{\pi}{2} - \arccos\left(\vec{pv} \cdot \vec{up}\right), \tag{3.43}$$

$$\theta_{inc} = \arccos\left(-\vec{pv} \cdot \vec{up}\right), \tag{3.44}$$

where $\vec{pv}$ is the normalized pointing vector and $\vec{r_{geodetic}}$ is the normalized vertical geodetic position vector. The subtraction is necessary because, as illustrated in Fig. 3.15, the arccosine of the dot product yields the complementary angle to the incidence angle.

3.2.9 Relative Azimuth Angle

The relative azimuth angle θ_{az} is calculated with respect to north at a point on the surface (generally the intersection of the pointing vector and the surface). The pointing vector is first converted to the NED frame utilizing a matrix created as described in Section 3.2.1. The azimuth angle is then calculated utilizing just the North and East components of the vector:

$$\theta_{az} = \arctan\left(\frac{pv_E}{pv_N}\right), \tag{3.45}$$

where pv_N and pv_E are the North and East components of the converted pointing vector, respectively.

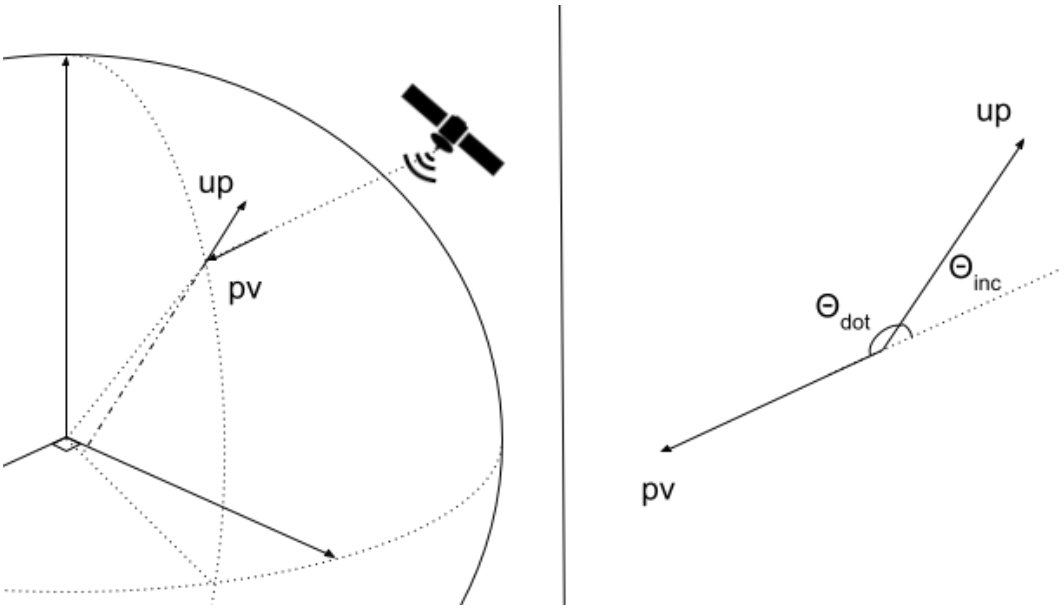

Figure 3.15: Illustration of the vectors and angles involved in the computation of the incidence angle. The vector $\vec{pv}$ is the unit pointing vector and the vector $\vec{up}$ is the unit up vector at the intersection point with the Earth's surface. θ_{dot} is the angle calculated using the dot product of the two vectors, while θ_{inc} is the incidence angle which is shown to be complementary to θ_{dot}.

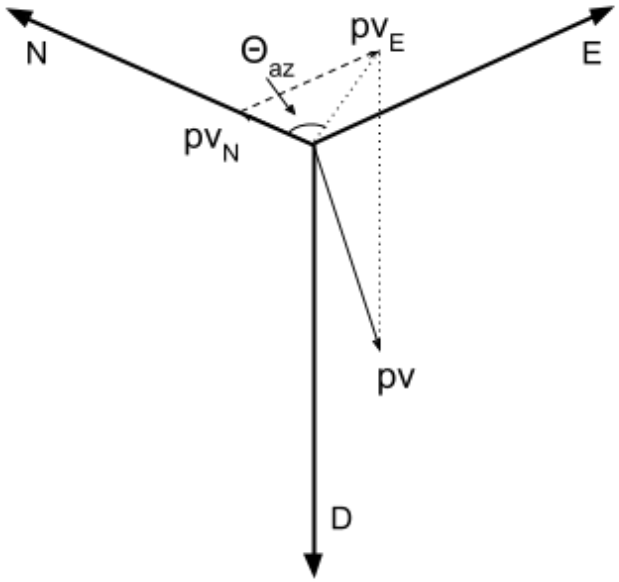

Figure 3.16: Illustration of the calculation of relative azimuth angle with respect to north. A vector's North and East components in the NED frame are the only necessary information to calculate θ_{az}

3.2.10 Doppler Frequency Shift

The Doppler frequency shift at a point on the Earth's surface is defined as

$$f_d = \frac{2}{\lambda}\vec{v_r} \cdot \vec{\mu}, \tag{3.46}$$

where λ is the wavelength of the transmitted frequency (which is equal to the frequency divided by the speed of light), $\vec{v_r}$ is the relative velocity vector between the spacecraft and the point, and $\vec{\mu}$ is a unit vector between the spacecraft and the point.

3.3 Conclusion

The software package containing all of these calculations forms the backbone of the GLOWS modeling framework. All of the code was tested thoroughly against the old software to ensure that the same or better results were achieved in both accuracy and speed. The rest of this thesis and future work on GLOWS (or other spacecraft missions) at BYU can rely on this package for doing higher level analysis of the mission.

CHAPTER 4. VALIDATION OF INSTRUMENT REQUIREMENTS

The tools of Chapter 3 allow for the analysis of the ability of the GLOWS mission to meet the mission requirements discussed previously in Section 2.3.1. GLOWS is attempting to meet all of the same performance requirements as SMAP by meeting the same instrument requirements. In this chapter, justification is developed for the instrument requirements and how they achieve the mission measurement requirements.

4.1 Orbit and Coverage

The decision with the largest impact on the mission's ability to meet the its requirements is the selection of an orbit. GLOWS will be placed into the same orbit as SMAP. The main measurement requirements that influence this decision are the requirement to have samples at a consistent local time of day, and to have global coverage every 3 days.

4.1.1 Consistent Timing of Observations

The requirement on the consistent local time of day of samples is to ensure consistency in the data set. If measurements are taken at different times of day, any number of factors could influence the measurements and there could be much more noise to account for. Consistency is always helpful in interpreting measurements of complex systems. The specific local time of day chosen is 6 AM/6 PM. This time of day was chosen to minimize Faraday rotation and to allow for easier estimation of soil temperature by use of air temperature.

Faraday rotation is the rotation of the polarization of an electromagnetic wave as it travels through a charged medium. The polarization rotation affects the purity of the measurements at each polarization and is difficult to compensate for. In the Earth's atmosphere this rotation mainly happens in the ionosphere. The magnitude of the effect depends on the total electron count in the ionosphere, which is minimized around 6 AM [6]. Choosing an

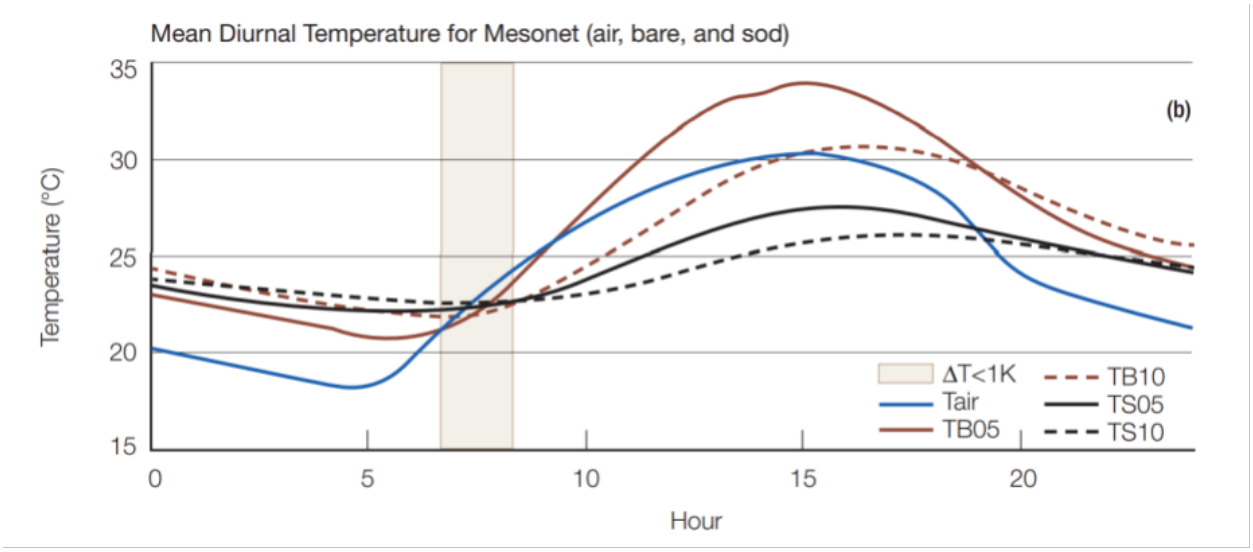

Figure 4.1: Mean temperature of the air, bare soil at depths of 5 and 10 cm, and sod covered soil at the same depths. The highlighted portion shows the times when the difference between all of the temperatures is less than 1 K. Taken from [6].

orbit with observations at this time minimizes the amount of correction that may need to be done.

The hours around dawn have also been found to be when the temperature is most consistent between the air and the ground. This is shown in Fig. 4.1. The temperature of the air, bare soil, and sod-covered soil are all within 1 K of each other on average around 6 or 7 AM. This is helpful because the estimate of the soil's emissivity from the radiometer measurements depends on its physical temperature. Unfortunately, the soil temperature is not measured at most locations on the Earth. The air temperature, however, is measured and modeled everywhere for weather predictions. Taking measurements at the time where air and soil temperature are roughly equal allows for the use of the known air temperature in place of the unknown soil temperature. It is also shown in [6] that this assumption is true for different depths of soil at this time of day.

The type of orbit that allows for measurements at a consistent local time of day is known as a sun-synchronous orbit. The inclination and altitude of the orbit combine such that the precession of the orbital plane around the Earth happens at the same rate as the Earth rotates around the sun. This ensures that the sub-orbital (or nadir) track of the

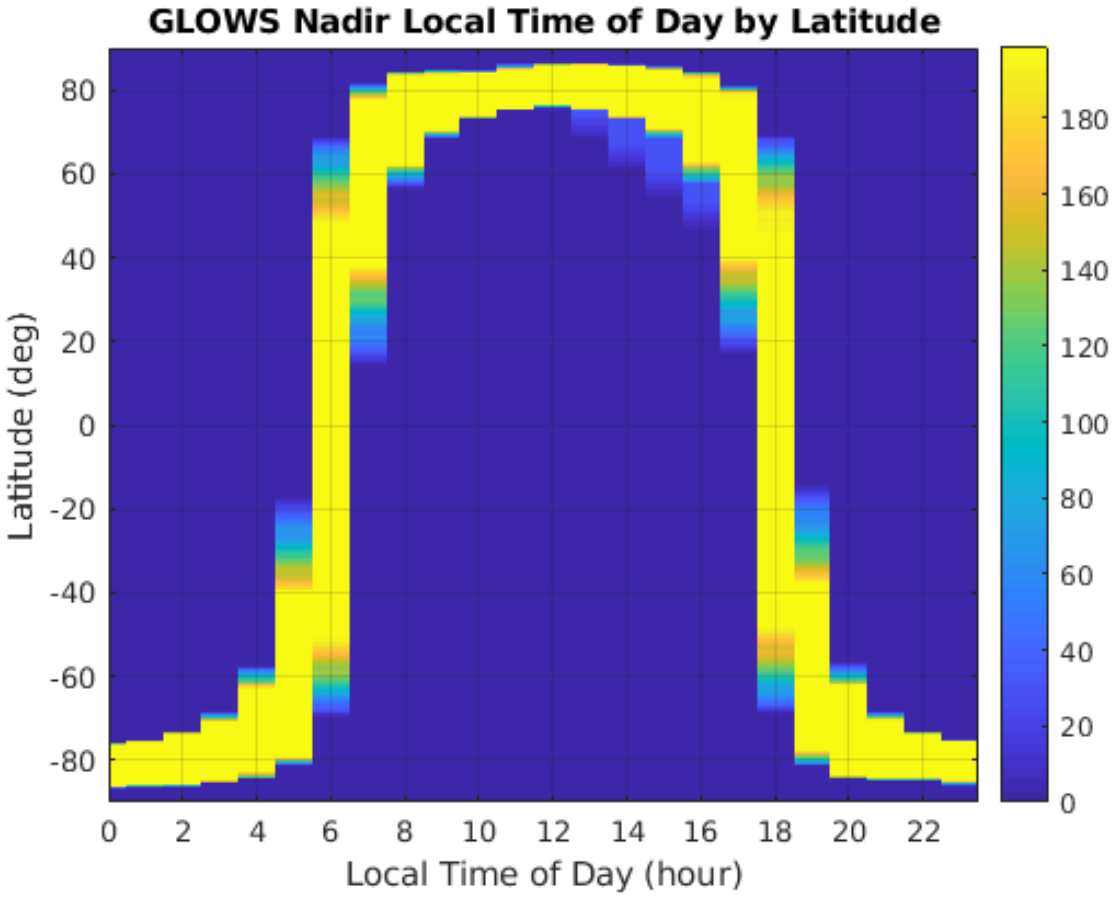

Figure 4.2: Histogram of local time of day of GLOWS measurements over the span of 1 year. The histogram stays consistent due to the sun-synchronous orbit.

satellite is always at the same local time of day (12 hours apart on opposite sides of the orbit).

Using orbit propagation software in conjunction with the observation geometry software, Fig. 4.2 shows the local time of day of observations by GLOWS in the same orbit as SMAP over the course of a whole year. To simplify processing, measurements were only analyzed from every 30 days. The figure clearly shows that the local time of day is consistent throughout the whole year and is at 6 AM/6 PM at the equator. Selecting the same orbit as SMAP enables GLOWS to achieve the same time of day for its measurements to enable continuity of the SMAP data set.

4.1.2 Revisit Period

To verify that the whole Earth is covered every 3 days, the orbital propagation and geometry program was run for three days. The number of times an area was observed in the simulation is shown in Fig. 4.3. In (a) the SMAP look angle of the antenna (35.5°) is used, while in (b) a look angle of 30° is used. Using the same look angle as SMAP does achieve full coverage in 3 days, while using the shallower look angle leaves gaps in coverage near the equator which can be seen in the deepest shade of blue in the figure. When the simulation runs for only 2 days worth of observations clearly shows that there are no gaps above 45° N, so the 2 day Boreal revisit requirement for freeze/thaw state is met as well. GLOWS will utilize the same orbit and look angle to meet the requirements.

4.2 Spatial Resolution

With the orbit and antenna look angle selected to meet temporal requirements, attention is turned to ensuring that spatial resolution requirements are met.

4.2.1 Radiometer

For the radiometer this depends entirely on the footprint size on the ground of the antenna. As is typical in remote sensing, the footprint is defined as the area inside the 3 dB contour of the antenna pattern on the ground. The scanning of the antenna introduces some more complexity because the antenna pattern is moving while the radiometer is performing the integration involved in each measurement. The GLOWS radiometer, like the SMAP radiometer, will use 12 consecutive integration windows to create each measurement (see Section 2.3.2). Figure 4.4 illustrates each of the 12 footprints involved in a measurement in range (from the nadir point) and distance along the scanning direction using the nominal SMAP beamwidth of 2.7° and rotation rate of 14.6 rpm [6]. Each individual footprint is shown to be an ellipse with a major axis of approximately 52 km and a minor axis of approximately 40 km. While this appears to violate the 40 km resolution requirement for radiometer measurements, the requirement is actually in terms of area. The area of the footprint is 1600 km^2 which is equivalent to a 40 km square measurement.

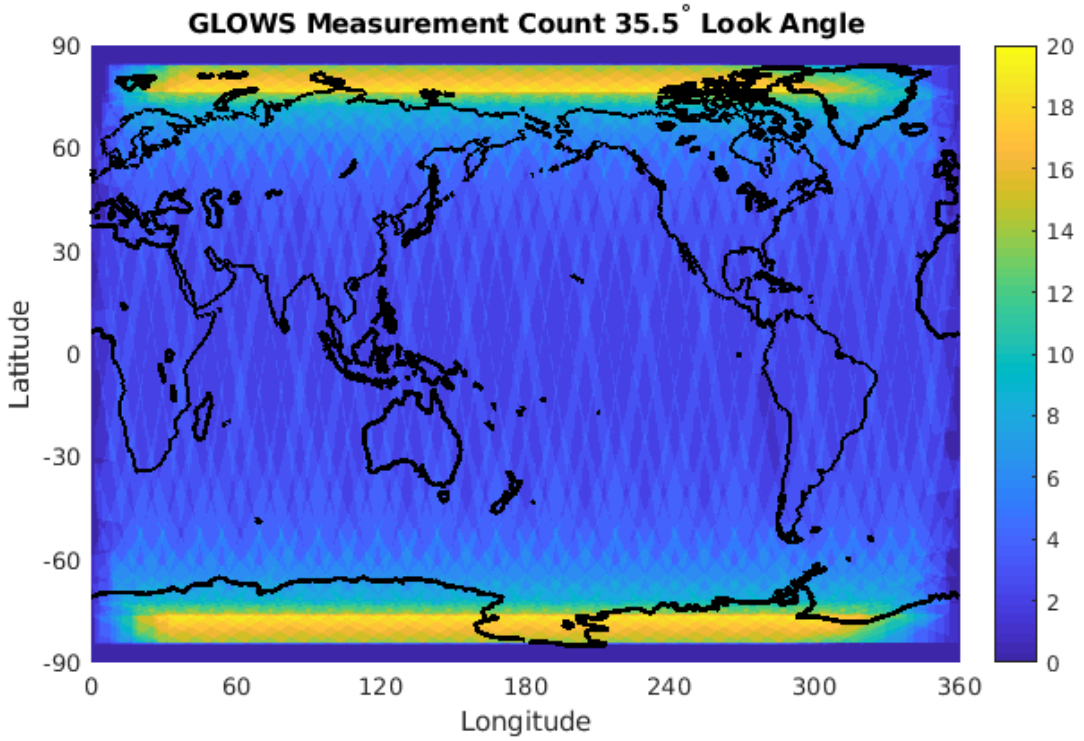

(a)

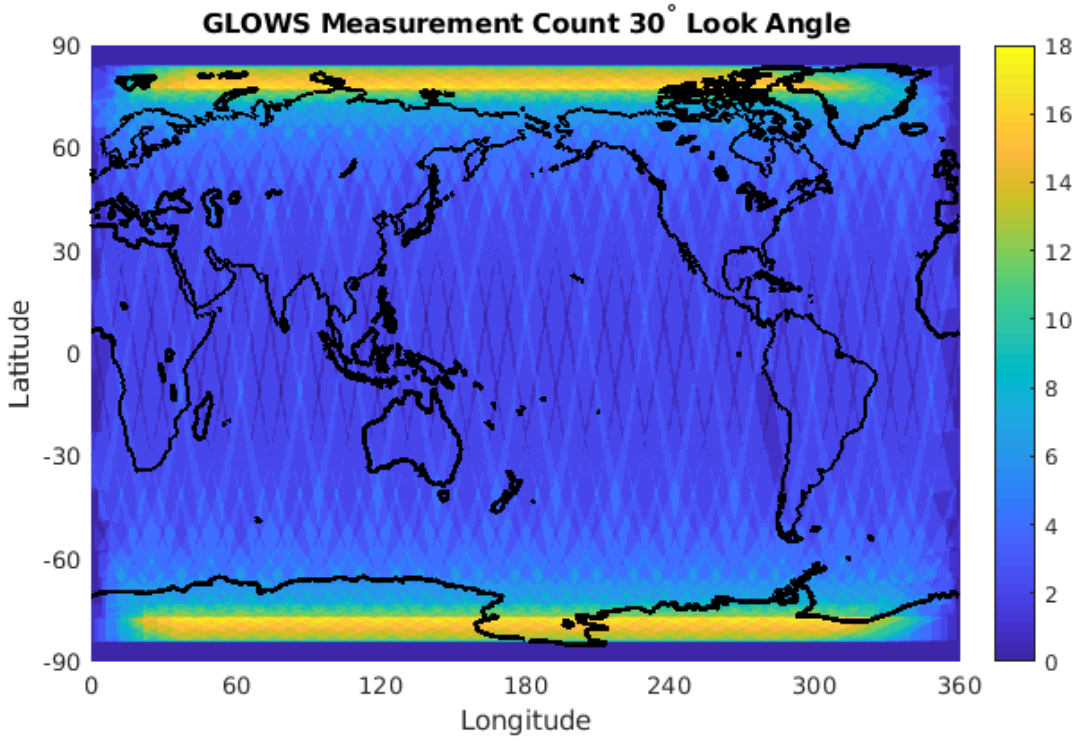

(b)

Figure 4.3: Observation counts for each location on Earth after 3 days with antenna look angles of 35° in (a) and 30° in (b). Note in (b) the gaps with no observations near the equator.

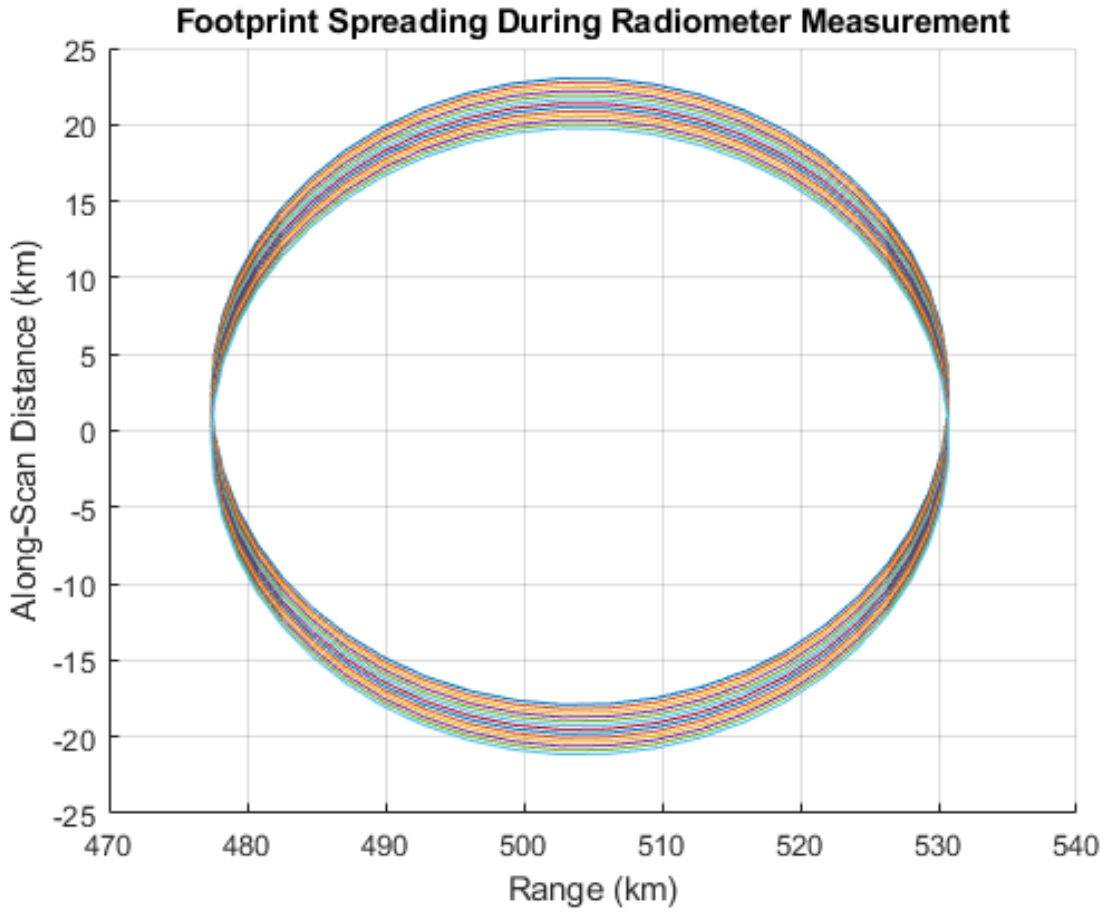

Figure 4.4: The 3 dB antenna footprint of the radiometer for each of the 12 integration windows in one radiometer measurement.

Although an instantaneous footprint appears to meet the 40 km resolution requirement, the scanning of the antenna could cause the area to increase beyond the requirement. As shown in Fig. 4.4, the antenna rotation causes approximately 4 km worth of spreading in the along-scan direction, while there is no change in the range direction. This spreading is relatively negligible, especially because the effective antenna pattern of all of the measurements combined likely has a 3 dB contour that is smaller than the overlaid footprints shown in the figure. Based on the criteria used for SMAP, as long as the GLOWS lens antenna can achieve the same beamwidth as SMAP's antenna, then the radiometer can achieve a 40 km resolution for its measurements.

4.2.2 Radar

The radar measurements have two different resolution requirements: 10 km or less for hydrometeorology and 3 km or less for freeze/thaw state. Clearly what matters is that the radar can achieve the tighter requirement of 3 km resolution. Both of these requirements are for the SAR processed measurements. SAR resolution for a rotating antenna SAR is defined in [10] as

$$\delta_{\text{el}} = \frac{c}{2 \sin \theta_{\text{inc}} B_t} \tag{4.1}$$

and

$$\delta_{\text{az}} = \frac{R\lambda}{2 v_{\text{sc}} \tau_d} f(\theta_{\text{az}}), \tag{4.2}$$

where δ_{el} and δ_{az} are the elevation and azimuth direction resolutions, respectively; c is the speed of light; θ_{inc} is the incidence angle; B_t is the bandwidth of the radar pulse; R is the slant range to the target; λ is the wavelength of the pulse; v_{sc} is the spacecraft velocity; τ_d is the synthetic aperture time; θ_{az} is the azimuth angle of the antenna; and $f(\theta_{\text{az}})$ is the degradation in resolution due to squint elongation. This degradation is shown in Fig. 4.5. If the antenna is looking perpendicular to the spacecraft velocity the iso-range and iso-Doppler lines are nearly perpendicular allowing for maximum resolution, while if the antenna is looking in the direction of the spacecraft velocity, the iso-range and iso-Doppler lines are parallel and the only resolution possible is range resolution. The degradation function scales the azimuth resolution of the perpendicular case based on the antenna azimuth angle.

Using Eq. 4.1 and substituting in a 40° incidence angle (which corresponds to the 35.5° antenna look angle) with the 1 MHz bandwidth which GLOWS and SMAP use yields an elevation/range resolution of approximately 233 m. This resolution is constant no matter the azimuth angle (it is the distance between the concentric circles in Fig. 4.5), but the azimuth resolution varies greatly with azimuth angle as shown in Fig. 4.6. Because of the deterioration in resolution close to the center of the swath, SAR data is only collected over the 70% of the swath [11]. Another feature of the processing that mitigates the effect of the resolution deterioration is multilooking. The resolution shown in Fig. 4.6 is that of a single look (a technical term in radar meaning one output of the processor). Several looks are binned together in a 1 km grid and averaged in the SMAP SAR processing [11]. This

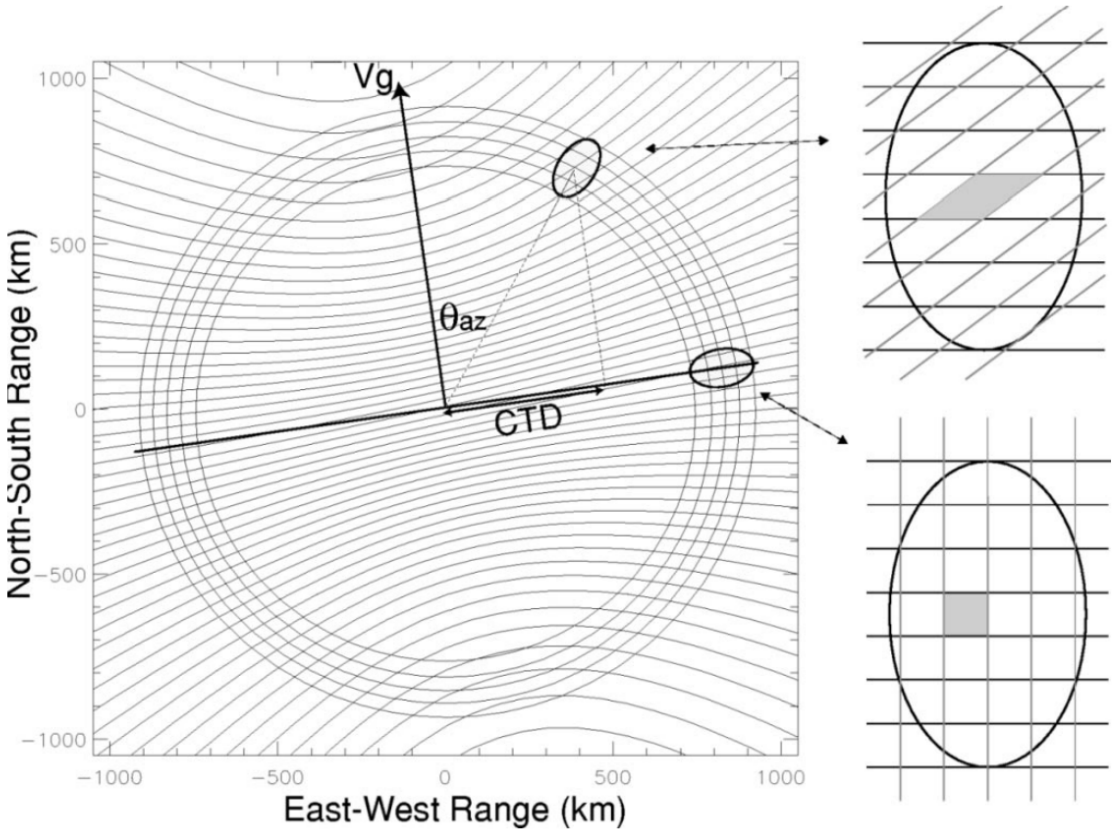

Figure 4.5: Illustration of the dependence of SAR resolution on azimuth angle. Taken from [10].

reduces the variance of the measurements and makes the effects of the single look resolution essentially negligible. The resolution has been averaged out to the 1 km grid. This meets the 3 km requirement.

4.3 Brightness Temperature and Soil Moisture Uncertainty

Knowing that GLOWS can achieve high resolution measurements is important, but if the measurements are uncertain, they are not very useful. GLOWS, like SMAP, is required to achieve less than 0.4 m^3/m^3 (1-σ) uncertainty level in soil moisture measurements. To ensure that this is possible the soil moisture uncertainty must be traced back to uncertainties in the quantities used to calculate it. These quantities include the brightness temperature as well as several ancillary data sets such as the surface temperature, soil composition, and vegetation water content (VWC). Each of these inputs to the algorithm to calculate soil

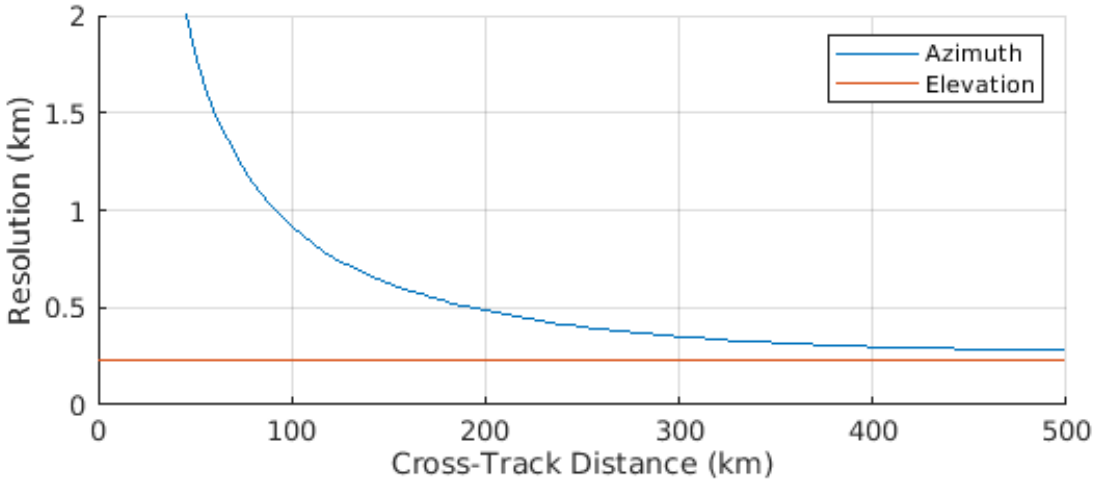

Figure 4.6: The resolution in azimuth and elevation by cross-track distance for GLOWS.

moisture have different uncertainty levels which affect the uncertainty of the soil moisture measurements.

4.3.1 SMAP Results

The SMAP team characterized the effects of uncertainty in each of the inputs to the soil moisture algorithm with a sophisticated global simulation of SMAP measurements [12]. They fed the data with added error in each of the necessary parameters into the four different algorithms and found the resulting error in soil moisture. Figure 4.7 summarizes the results of feeding errors in all of the parameters individually and taking the root sum of squares (RSS) of each of the root mean squared errors (RMSE) of the algorithms. Figure 4.8 shows the effect of using all parameters with error simultaneously in each of the algorithms. The simultaneous error raised the overall RMSE of each of the algorithms compared to the estimate using the RSS of each individual error. The simultaneous uncertainty simulations also show that the uncertainty increases past the allowed 0.04 m^3/m^3 as the VWC gets close to 5 kg/m^2, so SMAP can only achieve the required soil moisture uncertainty below that VWC level.

	Baseline	Option 1	Option 2	Option 3
Model/Ancillary Uncertainty	SCA (H) RMSE (cm^3/cm^3)	SCA (V) RMSE (cm^3/cm^3)	DCA RMSE (cm^3/cm^3)	MPRA RMSE (cm^3/cm^3)
Gridding + Aggregation	0.00612	0.00581	0.00591	0.00582
5% h	0.00645	0.00595	0.00595	0.00583
5% omega	0.00629	0.00605	0.00619	0.00611
5% sand fraction	0.00729	0.00699	0.00702	0.00697
5% clay fraction	0.00615	0.00585	0.00594	0.00585
2K T5	0.00871	0.01000	0.01120	0.01200
5% VWC	0.00656	0.00608	–	–
10% VWC	0.00717	0.00647	–	–
5% water fraction	0.00612	0.00582	0.00591	0.00582
10% water fraction	0.00612	0.00582	0.00591	0.00583
20% water fraction	0.00614	0.00584	0.00593	0.00583
1.3 K TB	0.00681	0.00674	0.00828	0.00951
RSS	0.0203	0.0201	0.0205	0.0214

Based on GloSim.

Figure 4.7: The RMSE of the various algorithms used to recover soil moisture from SMAP radiometer data due to error in only the parameter listed on the left. Taken from [12].

4.3.2 Validation for GLOWS

To validate these results, mainly in the effect of brightness temperature, Former MERS student Jordan Brown's implementation of the single channel (SCA) algorithms is used since the SMAP algorithm is not currently available [13]. In order to provide valid combinations of all of the parameters necessary to the algorithm, parameters are taken from actual SMAP measurements. Then, Monte Carlo simulation is performed by creating a normal random variable with a mean of the reported T_B and standard deviation of 1.3 K. One million realizations of the random variable are passed along with the reported ancillary data to the soil moisture algorithm. The resultant soil moisture measurements are analyzed to determine the distribution and after doing this for several sets of brightness temperature and ancillary data, the RMSE of the algorithm is determined.

After limiting the samples taken from SMAP to only those with vegetation water content less than or equal to 5 kg/m^2, the resulting standard deviations of soil moisture are plotted against the VWC in Fig. 4.9. The plot shows a clear positive correlation between VWC and uncertainty in soil moisture, just as in Fig. 4.8. The overall RMSE from these

L2_SM_P Error Analysis								
	h	omega	sandfrc	clayfrc	T5	VWC	watrfrc	TB
RMSE	5%	5%	5%	5%	2 K	5%	10%	1.3 K

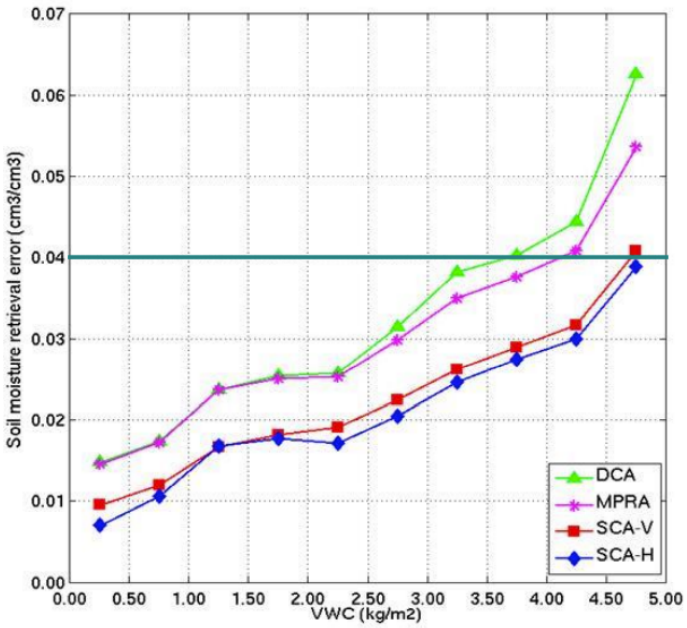

RMSE averaged across all VWC bins			
SCA-H	SCA-V	DCA	MPRA
0.0213	0.0227	0.0323	0.0305

Figure 4.8: The RMSE of the different algorithms shown given the errors in all inputs shown in the table labeled "L2_SM_P Error Analysis" simultaneously. Taken from [12].

data is 0.00800 m^3/m^3, which is slightly higher than the 0.00678 m^3/m^3 average between the H and V algorithms from Fig. 4.7, but not worryingly so. For one thing, the algorithm used is not entirely the same, but GLOWS will be sure to use the same algorithm as SMAP. In addition, the SMAP results were taken from much more data than there was time to replicate in this study.

It appears that, assuming the rest of the SMAP simulation is accurate, a brightness temperature uncertainty of 1.3 K is sufficient to achieve the required soil moisture uncertainty. The key question for GLOWS is whether the change to a less efficient lens antenna will allow for the radiometer to still achieve that level of precision. The next chapter analyzes this topic in depth.

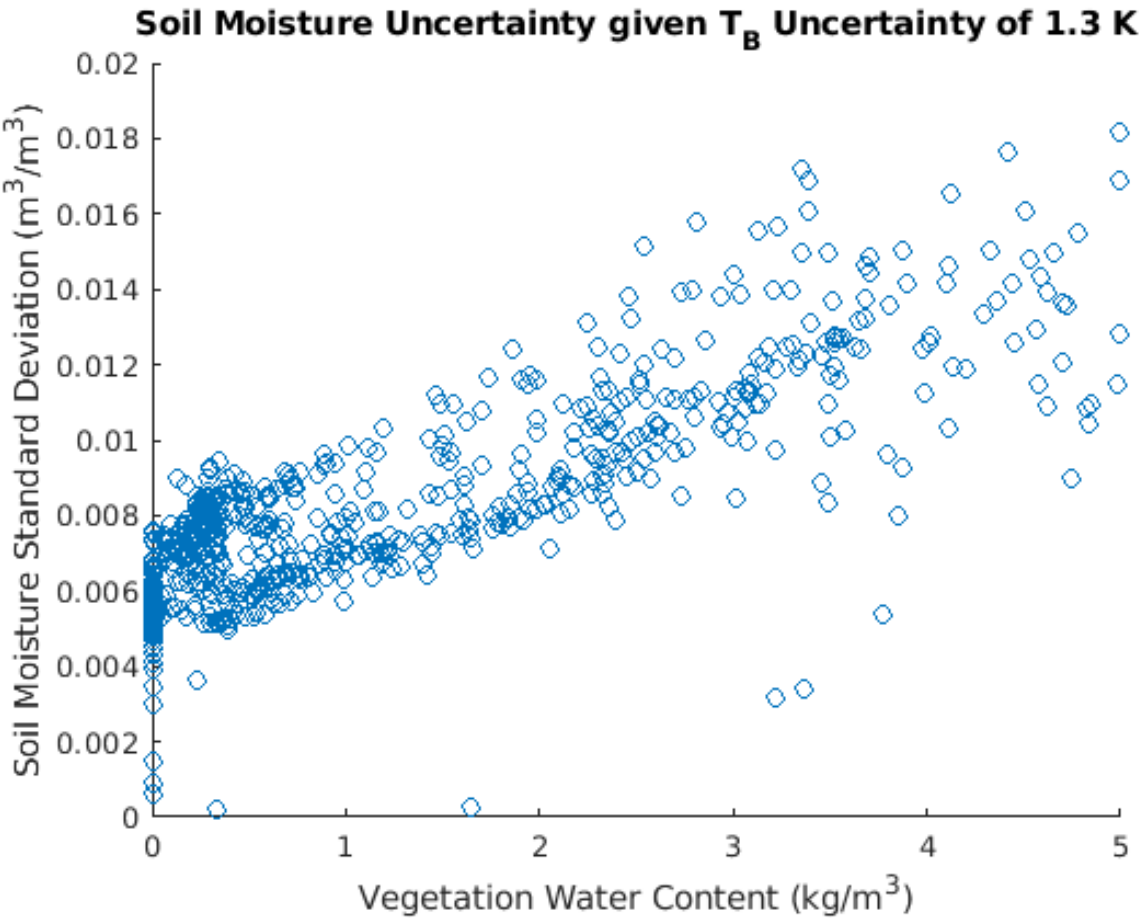

Figure 4.9: The standard deviation of the soil moisture output by Jordan Brown's algorithm versus vegetation water content, given a brightness temperature input with 1.3 K standard deviation and constants for all other inputs.

4.4 Summary

This chapter has considered the connections between the instrument requirements and the associated key measurement requirements. The approach for demonstrating that the instrument requirements are sufficient to meet the soil moisture measurement requirements has been presented.

CHAPTER 5. EFFECT OF LENS ANTENNA ON INSTRUMENT PERFORMANCE

5.1 Introduction

The switch from a reflector antenna on SMAP to a less efficient lens antenna on GLOWS introduces more uncertainty into the radiometer measurements. Radiometer measurements require especially precise calibration [14], a process made more difficult by using a more lossy lens instead of a reflector. The greater loss both attenuates the incoming signal and introduces more noise into the system that cannot be easily measured. Unlike noise sources internal to the receiver, antenna noise cannot be measured with use of a reference noise source and must be calculated from accurate knowledge of the physical temperature and electromagnetic characteristics of the antenna [1]. Accurately measuring the physical temperature is difficult because the lens is made of several layers that could be at different temperatures. Embedding sensors into the lens would alter the electromagnetic properties that make the lens work. Instead, the temperatures of the layers must be modeled using measurements that can be taken. This modeling can be used to produce an effective temperature to represent the lens as a whole in a bulk model. In the remainder of the chapter the necessary accuracy and precision of this temperature model to ensure the radiometer measurements meet specifications are analyzed.

5.2 Derivations

A radiometer measures the apparent brightness temperature, T_A, of the scene in view of its antenna. The brightness temperature is the blackbody-equivalent temperature of the power of the naturally occurring electromagnetic radiation emanating from all objects as defined by Planck's radiation law. The apparent brightness temperature can be calculated

as a weighted average of the incoming brightness temperature by the antenna gain pattern:

$$T_A = \frac{\iint\limits_{4\pi} T_B(\theta,\phi)G(\theta,\phi)\,d\Omega}{\iint\limits_{4\pi} G(\theta,\phi)\,d\Omega} \tag{5.1}$$

where $T_B(\theta,\phi)$ is the incident brightness temperature from all angles and $G(\theta,\phi)$ is the antenna gain pattern. Because the antenna is not ideal, it attenuates T_A and creates additional noise power that is modeled as an equivalent brightness temperature. The temperature seen at the output port of the antenna due to these effects is represented as

$$T_A^{'} = \xi T_A + (1-\xi)T_p \tag{5.2}$$

where ξ is the radiation efficiency and T_p is the physical temperature of the antenna.

As the power in the signal transferred from the antenna to the receiver propagates through the radiometer system, the components of the system add additional noise power to the signal. This noise power is equivalent to an additional black-body temperature added to the temperature measured by the system yielding a total system temperature

$$T_{\mathrm{SYS}} = T_A^{'} + T_{\mathrm{REC}}^{'} \tag{5.3}$$

where $T_A^{'}$ is the temperature output of the antenna as defined in Eqn. 5.2 and $T_{\mathrm{REC}}^{'}$ is the equivalent temperature of the noise power added by the receiver. The goal is to recover T_A from T_{SYS} as accurately as possible. This can only be accomplished with accurate knowledge of T_{SYS} and all of the parameters that define $T_A^{'}$. Most radiometers continuously measure $T_{REC}^{'}$ using a known reference load instead of the antenna to remove the bias caused by the receiver. To recover T_A from $T_A^{'}$ then requires knowing only the antenna efficiency and physical temperature. If the efficiency is high enough, the sensitivity to the physical temperature may be low enough that it could even be neglected. Calibrating the system in this way removes the bias of the instrument and improves the accuracy of the reported temperature.

As in all scientific measurements, the reported temperature has a precision as well as the accuracy. The precision is how close together measurements of the same quantity are, and is often described in radiometry as the smallest change in input temperature that can be detected. The precision is also termed radiometric sensitivity or radiometric resolution. For an ideal total-power radiometer with no gain fluctuations, the precision is defined as

$$\Delta T_{\mathrm{IDEAL}} = \frac{T_{\mathrm{SYS}}}{\sqrt{B\tau}} \tag{5.4}$$

where T_{SYS} is given in Eqn. 5.3, B is the bandwidth of the receiver, and τ is the measurement integration time.

How does this change when the antenna includes a multi-layer lens? The multiple layers are modeled as a series of antennas that receive the signal and reradiate to the following layers. This changes the derivation of $T_A^{'}$ because T_A is attenuated and noise is added by all of the antennas not just one, and they may all have different characteristics. For a lens of n layers

$$T_{\mathrm{LENS}}^{'} = \left(\prod_{i=1}^{n} \xi_i\right) T_A + \sum_{i=1}^{n} \left[\left(\prod_{j=i+1}^{n} \xi_j\right)(1-\xi_i)T_{p_i}\right] \tag{5.5}$$

where $T_{\mathrm{LENS}}^{'}$ is the equivalent brightness temperature reradiated by the lens, and ξ and T_p are the same as in Eqn. 5.2, but have now been indexed by the layer number. This relationship shows that T_A is attenuated by each layer and each layer adds noise based on its efficiency and physical temperature that is attenuated by each layer it passes through. Because the signal is traveling through the lens rather than bouncing off of a reflector, the efficiency terms are guaranteed to be relatively lower, so the additional noise terms related to the physical temperature cannot be neglected.

This brightness temperature is not passed directly into the receiver, instead it is passed through a feed antenna first. This further complicates the calculations because the lens brightness temperature could be different at different points and must all be weighted by the feed gain pattern. The equivalent brightness temperature observed by the feed can

Model.png Model.png

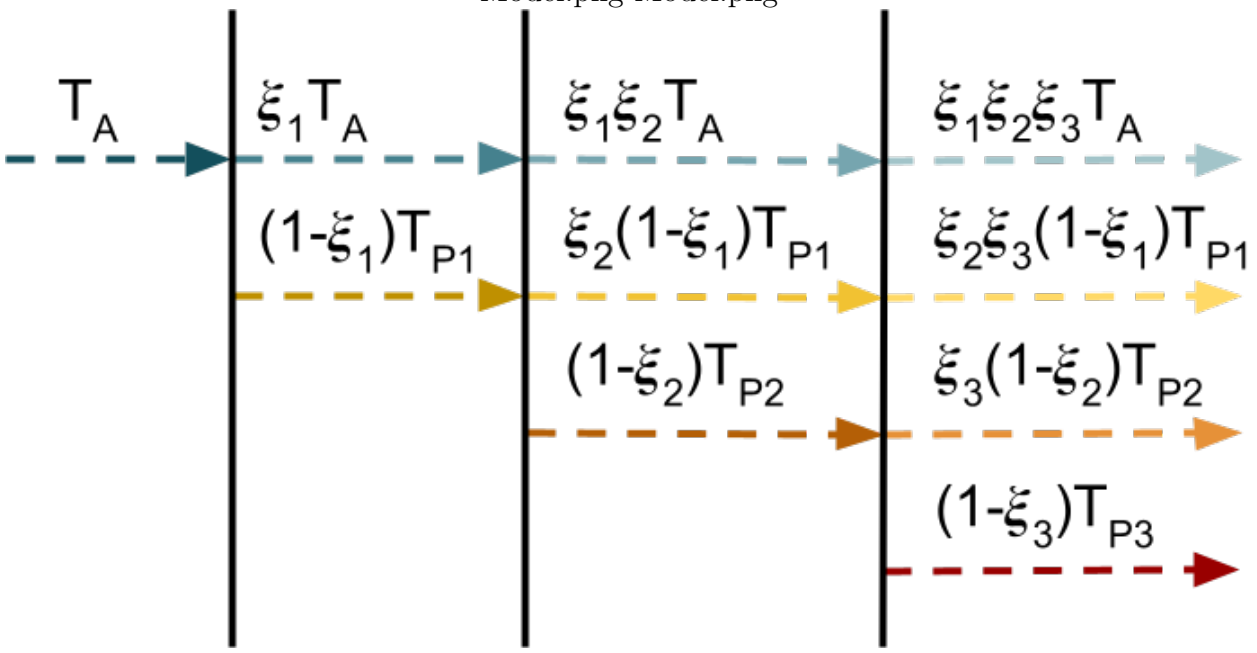

Figure 5.1: Graphical representation of T'_{LENS}. The self-emission of each lens layer is represented by a new arrow, and the attenuation of each signal by subsequent layers is represented by a lightening of the arrow and the addition of the efficiency term of the layer causing the attenuation.

be modeled as

$$T_{A_{\text{FEED}}} = \frac{\iint\limits_{\text{LENS}} T'_{\text{LENS}}(\theta,\phi)G(\theta,\phi)\,d\Omega}{\iint\limits_{\text{LENS}} G(\theta,\phi)\,d\Omega} + \frac{\iint\limits_{4\pi-\text{LENS}} T_B(\theta,\phi)G(\theta,\phi)\,d\Omega}{\iint\limits_{4\pi-\text{LENS}} G(\theta,\phi)\,d\Omega} \tag{5.6}$$

where $T'_{\text{LENS}}(\theta,\phi)$ is the brightness temperature at each specific point on the lens as viewed by the feed and everything else is the same as in the previous equation. $T'_{\text{LENS}}(\theta,\phi)$ is calculated assuming a linear path through the lens layers, meaning that it uses the physical temperatures of the layers at the same point. $T_{A_{\text{FEED}}}$ is substituted in for T_A in Eqn. 5.2 to yield

$$T'_A = \xi_{\text{FEED}} T_{A_{\text{FEED}}} + (1-\xi_{\text{FEED}}) T_{p_{\text{FEED}}} \tag{5.7}$$

for an antenna system comprised of a lens and feed.

(4).png (4).png

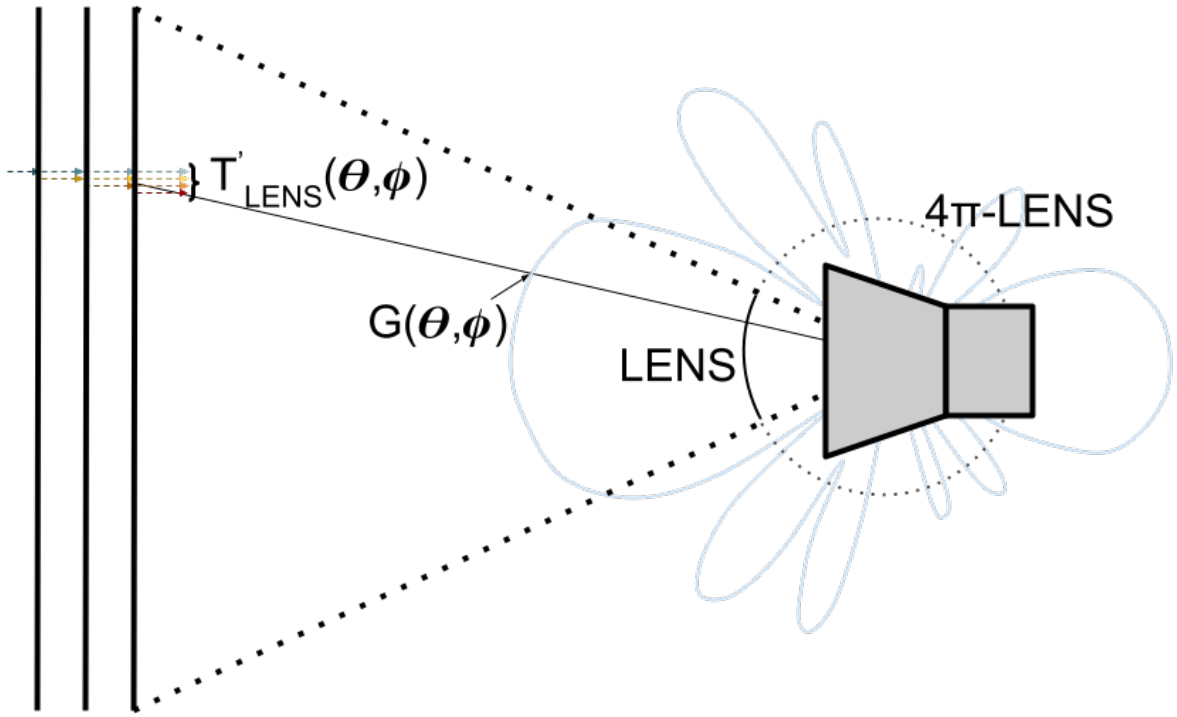

Figure 5.2: Illustration of quantities involved in $T_{A_{\text{FEED}}}$. The light blue notionally represents the gain pattern of the feed. The region between the two dashed lines (shown in 2D, but in reality a 3D region) represents the portion of the feed gain pattern intercepted by the lens. At each angle (θ, ϕ) both the gain pattern and the closest lens layer are intersected at exactly one point. T'_{LENS} at this point on the lens is calculated using the physical temperature at this same point on each layer of the lens (represented by the arrows from Fig. 5.1). The rest of the gain pattern is the $4\pi -$ LENS region (again, a 3D region represented in 2D in the figure) which views the apparent brightness temperature from other sources such as the Earth, Moon, and deep space.

5.3 Uncertainty

The derived model of the brightness temperature observed by the lens antenna system is used to determine what effect errors in the measurement/modeling of the physical temperature of the various lens layers has on the uncertainty of the radiometer measurements. As far as precision is concerned, the lens architecture is intrinsically less precise than a reflector antenna because of the increase in T_{SYS} caused by the loss of the lens material at its physical temperature, but the exact precision depends on the physical temperature of the lens. There

is nothing that can be done to improve the precision other than improving the efficiency of the lens so that an increase in physical temperature causes a smaller increase in T_{SYS}.

The accuracy of the radiometric measurements depends on the accuracy of the physical temperatures derived from measurement/modeling. The error in the physical temperature of each layer i is represented as δT_{p_i} and this notation (use of δ) is adopted as the accuracy error in any quantity. Assuming that the other quantities involved in calculating the brightness temperature are known accurately, the error in the apparent brightness temperature output by the lens is given as

$$\delta T'_{\mathrm{LENS}} = \sum_{i=1}^{n} \left[\left(\prod_{j=i+1}^{n} \xi_j \right) (1 - \xi_i) \delta T_{p_i} \right], \tag{5.8}$$

and the error in the overall apparent brightness temperature to the lens and the feed is given as

$$\delta T_{A_{\mathrm{FEED}}} = \frac{\iint\limits_{\mathrm{LENS}} \delta T'_{\mathrm{LENS}}(\theta, \phi) G(\theta, \phi)\, d\Omega}{\iint\limits_{\mathrm{LENS}} G(\theta, \phi)\, d\Omega}. \tag{5.9}$$

The added temperature by the receiver, T'_{REC} is assumed to be calibrated accurately as well, so $\delta T_{\mathrm{SYS}} = \delta T_{A_{\mathrm{FEED}}}$. The accuracy of the overall system temperature is dependent only on the accuracy of the physical temperature measurements of the lens. In reality, other parameters may need to be included in determining δT_{SYS}, but in this investigation only the effect of physical temperature errors is considered.

5.4 Physical Temperature Uncertainty Effects

The derived temperature and uncertainty models can be used with various assumptions about measurement error to estimate the effects of potential sources of error and determine the best scheme for determining the physical temperature of the lens. This process begins with defining the true temperatures of the lens. To use realistic values, the temperatures of the lens layers at minimum and maximum (when they are fully eclipsed by the Earth or illuminated by the Sun, respectively) are estimated from a simulation (Fig. 5.3).

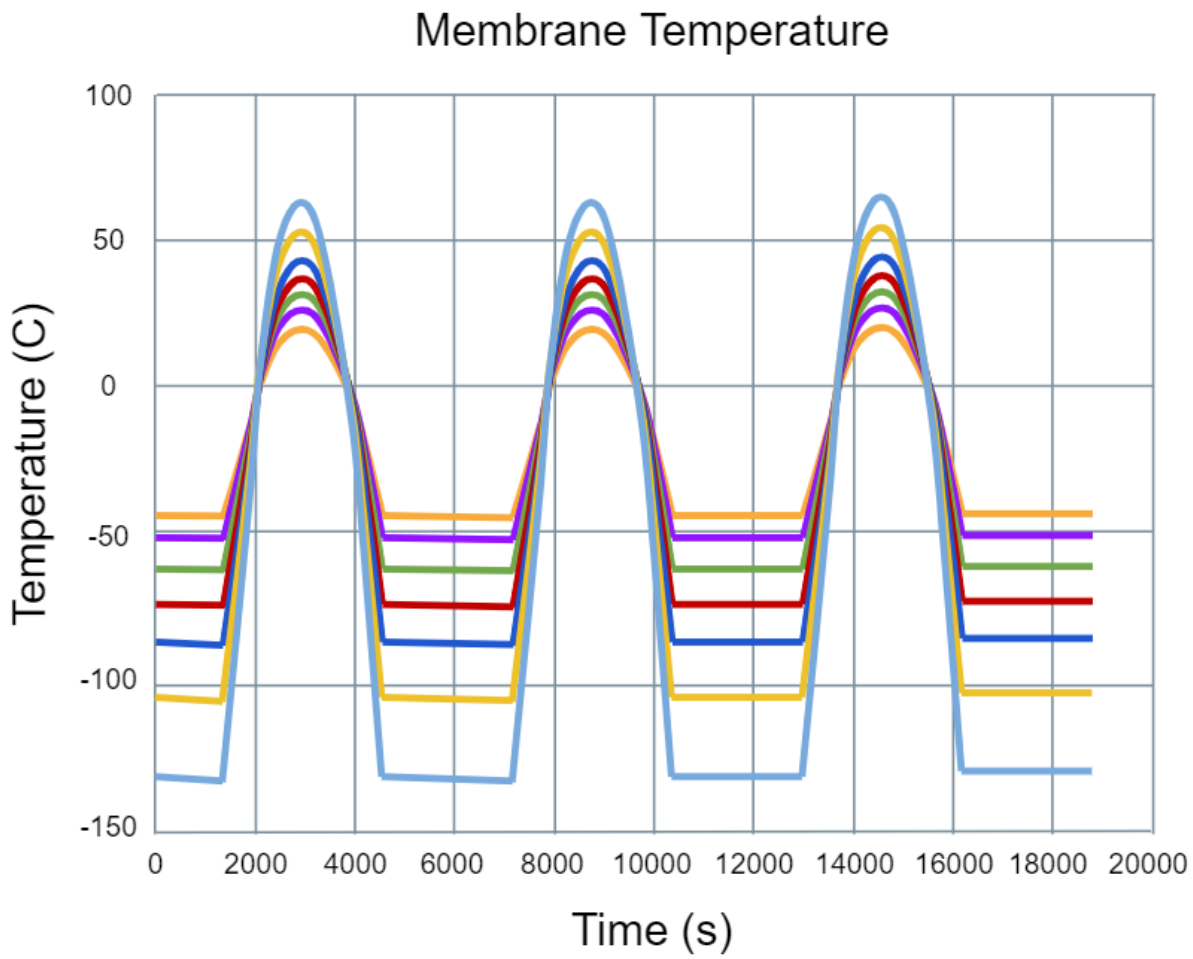

Figure 5.3: Representative plot of physical temperature as a function of time at the center of each layer of a 7-layer lens over three full orbits for simulation done by MMA Design, LLC. The layer closest to the spacecraft is the light blue line, while the layer closest to the Earth is the orange line. The other layers follow in order between them.

A further complication is that the temperature is not constant across each layer; there is some temperature gradient (Fig. 5.4). Because the feed does not uniformly illuminate the lens — it has its own gain pattern that weights the apparent temperature at each point on the lens — the temperature may need to be known not just for each layer, but for each point on each layer. To bound the problem, a linear gradient of 20 K is applied across each layer of the lens. This gradient is greater than the largest gradient seen in the simulation other than that caused by shadow. Using this gradient caused less than a 100 μK difference from a constant temperature model. This analysis suggests the the effect of the gradient across

Grads.png Grads.png

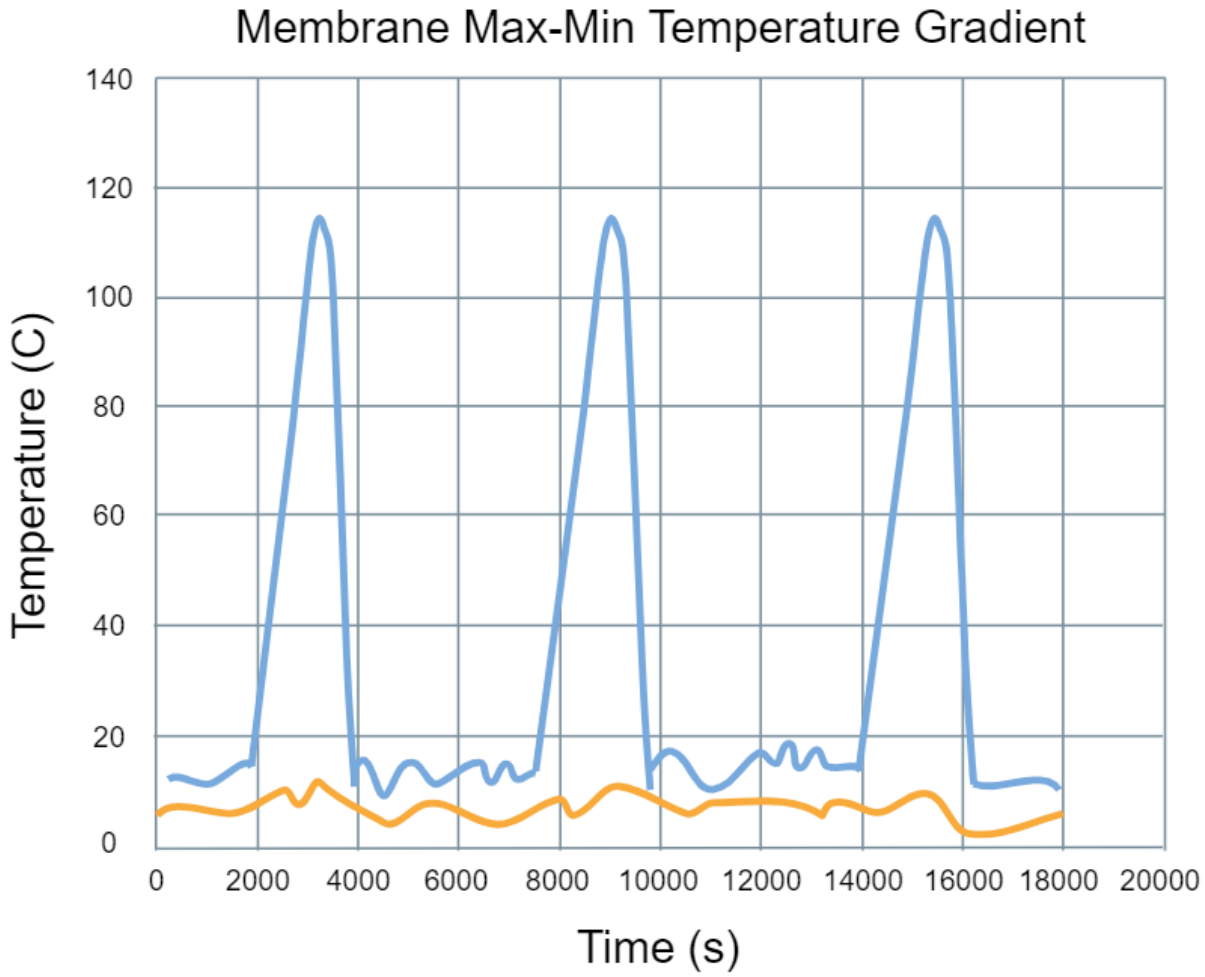

Figure 5.4: Representative plot of difference between maximum and minimum temperatures on the most inboard (closest to the spacecraft, blue) and outboard (closest to the Earth, orange) layers of the lens in the same simulation as Fig. 5.3. The spacecraft shadow is responsible for the spike in the gradient for the inboard layer.

the lens (for the expected normal gradients) is negligible and that a constant temperature can be assumed if there is no shadow.

However, depending on the spacecraft's orbit, the shadow of the spacecraft could pass over the lens. This could cause enough temperature gradient across some layers of the lens to ruin the assumption of constant temperature. Figure 5.5 shows the amount of change in the brightness temperature of self-emissions from a lens with no shadow to a lens with a shadow of various sizes. If the shadow is less than 10 percent of the diameter of the lens, then the difference is quite small and can be neglected depending on the accuracy requirements of

the system. If it gets much larger, though, the effect increases and may require a greater knowledge of the actual temperature distribution.

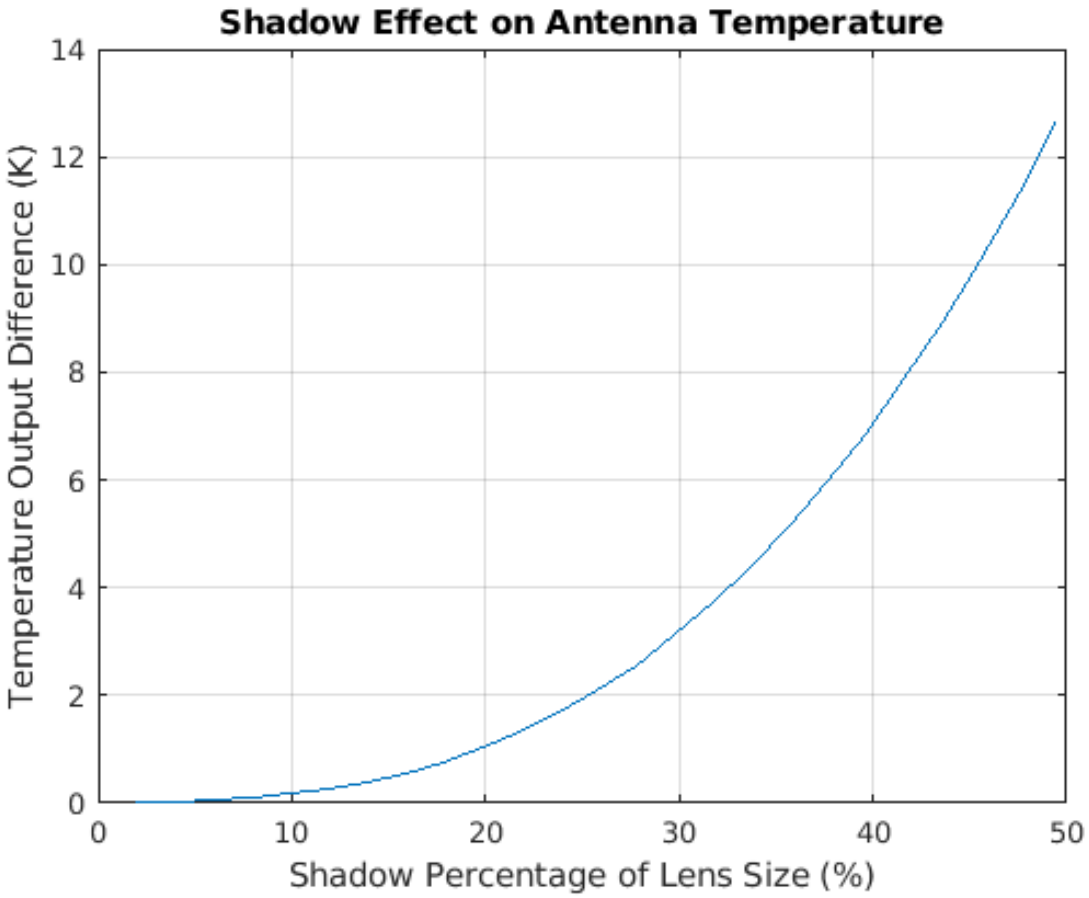

Figure 5.5: Estimated effect of shadow on the brightness temperature by size of the diameter of the shadow as a percentage of the diameter of the lens.

While assuming a constant temperature distribution across each layer of the lens is a helpful simplification, it does not remedy the issue of measuring or modeling that temperature for each layer. As noted previously, it is impossible to directly measure the temperature of each layer. Thermal sensors cannot be embedded in the lens without destroying the resonant properties that make it function. A thermographic camera could be mounted to the spacecraft but can only measure the temperature of the most inboard layer. Based on Fig. 5.3, that temperature may not be representative of the temperatures of every other

layer. The measurement of the most inboard layer could be used as an input to a model to calculate the temperatures of the other layers or perhaps to estimate the mean temperature.

Using the truth values taken from Fig. 5.3, the brightness temperature added by self-emission of the lens is calculate by setting T_A to 0 to only see the effect of the self-emission. The process is repeated using the top layer temperature for each layer. This approach is simple, but if it provides relatively accurate results it can be used. Unfortunately, the top layer is drastically cooler than the layer closest to Earth in eclipse and significantly warmer in illumination. The mean temperature is used instead and the resulting brightness temperature is much closer to the truth. In the specific example in Fig. 5.6, an overall loss of 0.5 dB is used for the lens. The resulting mean temperature has a maximum difference from truth of .1 K at eclipse. The difference changes depending on the loss of the lens, but this example suggests that so long as the mean is accurately known from some model, it could be sufficient.

Modeling the physical temperature of each layer is complicated, so it would be ideal to reduce the system to an equivalent model of a single equivalent physical temperature and the efficiency of the whole lens. This can be done by setting the self-emission terms from Eqs. 5.2 and 5.5 equal to each other:

$$(1-\xi)T_e = \sum_{i=1}^{n}\left[\left(\prod_{j=i+1}^{n}\xi_j\right)(1-\xi_i)T_{p_i}\right], \tag{5.10}$$

where T_e represents the equivalent physical temperature of the whole lens. Solving for T_e yields

$$T_e = \frac{\sum_{i=1}^{n}\left[\left(\prod_{j=i+1}^{n}\xi_j\right)(1-\xi_i)T_{p_i}\right]}{1-\xi}. \tag{5.11}$$

While this still relies on the physical temperatures of each layer to calculate directly, calibration of the instrument could be performed to determine the single parameter T_e as a function of the physical temperature of the most inboard layer much more easily and, potentially, accurately than the physical temperature of each layer. This is especially feasible if comparison with SMAP data is still possible as is planned currently. If the bulk model is used, the accuracy requirements can also be easily determined as a function of the efficiency

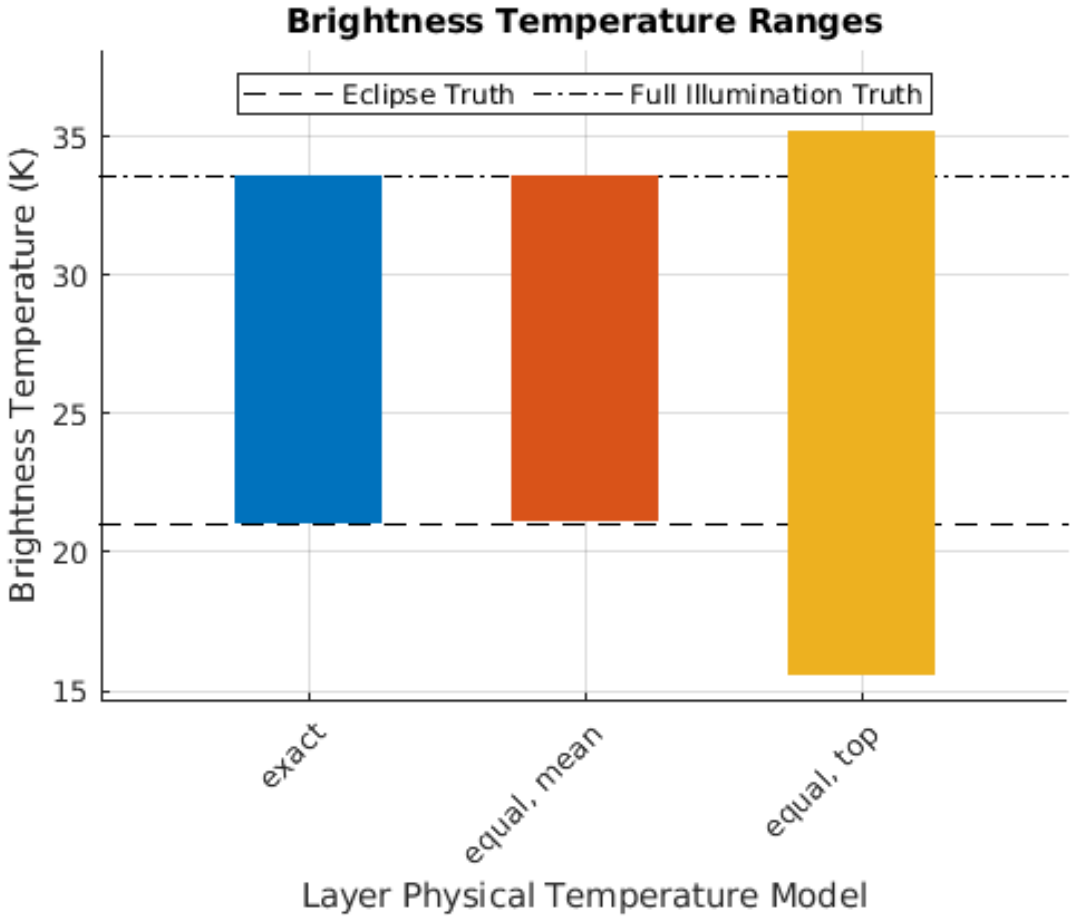

Figure 5.6: Comparison of brightness temperature ranges caused by the self-emission of the lens at various temperatures between eclipse and illumination using three different physical temperature models for the lens layers.

(or inversely, the loss) of the lens) as shown in Fig. 5.7. The slope of the lines can clearly be determined to be $(1-\xi)$ by inspection of Eq. 5.2, and ξ is the inverse of the loss. For a given loss of the lens it then becomes trivial to determine the necessary equivalent temperature accuracy to achieve a desired brightness temperature accuracy.

5.5 Analyzing Precision

As mentioned previously, the precision of the brightness temperature measurements made with the lens antenna system depends only on the resulting T_{SYS} caused by the physical temperature of the lens. Using the physical temperatures extracted from Fig. 5.3, the additional loss in precision ($\Delta T_{\mathrm{IDEAL}}$) expected at the extremes of the temperature ranges

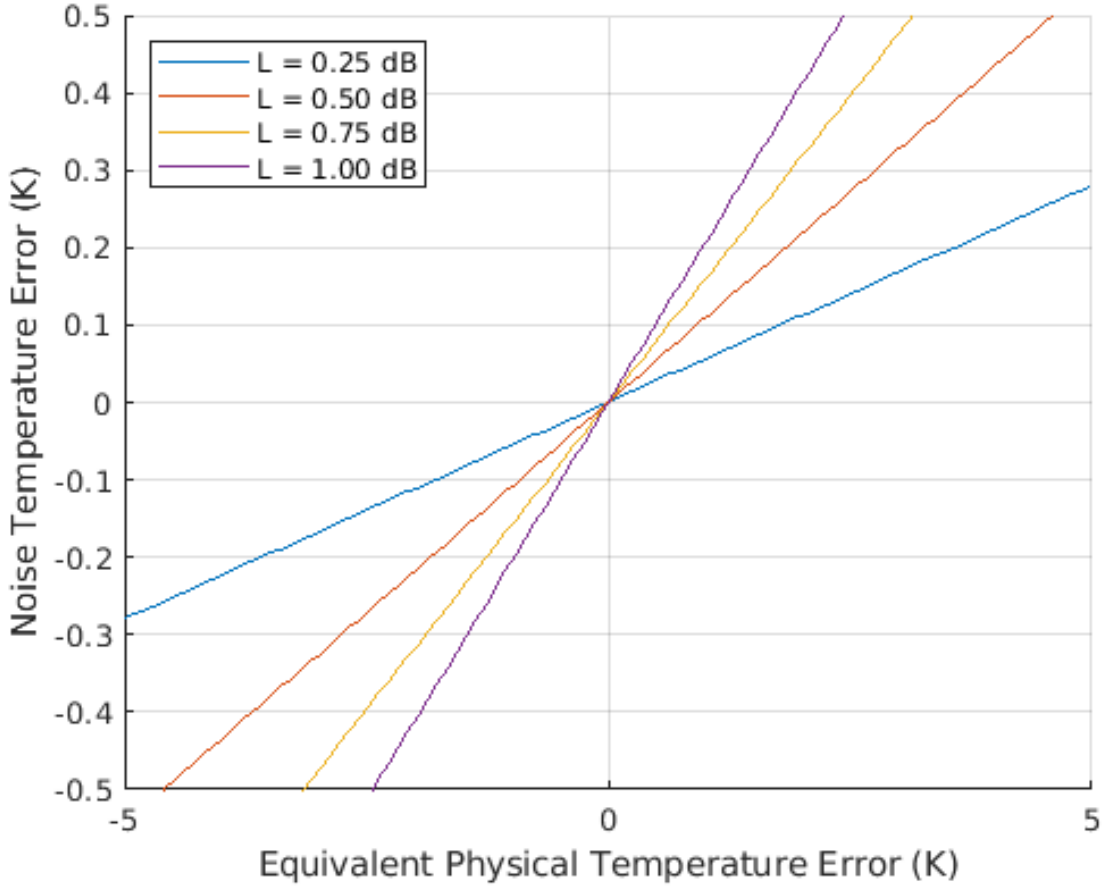

Figure 5.7: Comparison of the error in self-emission brightness temperature caused by error in equivalent physical temperature estimation for lenses of various losses. The relationship is a linear function, with the scale dependent on the lens loss.

can be calculated for various losses in the lens. The result of that calculation is represented in Fig. 5.8. It appears that with loss less than 0.8 dB, the lens never adds more than 0.1 K to the ΔT_{IDEAL} of the system. So long as the ΔT_{IDEAL} budget is large enough to allow for this, it appears that the precision degradation is not a significant concern.

5.6 Expected Antenna Errors for GLOWS

The theoretical results of the previous sections must be used with expected GLOWS lens parameters to estimate the uncertainty effects caused by the lens. To start with, it is assumed that the GLOWS radiometer receiver has the same noise performance as the SMAP

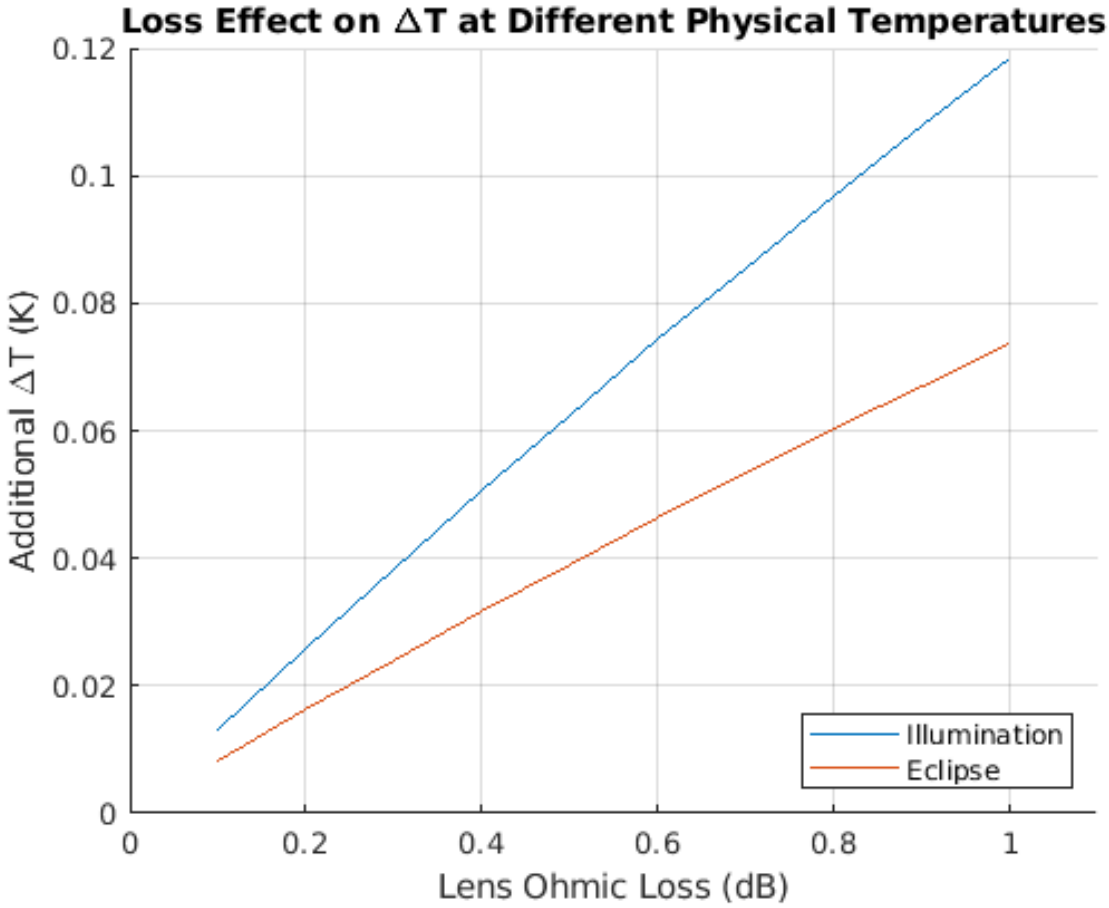

Figure 5.8: Effect of various losses through the lens on the precision of the radiometer measurements at extremes of the temperature ranges.

radiometer since the design is essentially the same. In terms of accuracy and precision, SMAP achieved 0.95 K precision and 0.62 K calibration stability (accuracy) [15]. The RSS of these terms is 1.1 K which meets the 1.3 K requirement, and leaves a little bit of room to allow for extra error caused by the GLOWS antenna loss.

The tricky part of estimating the antenna effects is that the loss is not known yet because the antenna is still in development. Both the accuracy and precision of the radiometer depend heavily on the loss of the lens, so results are analyzed over a range of losses. The error in the modeling of the lens temperature, however, has been determined to be dependent mostly on the uncertainty in the solar radiation levels and Earth albedo. The estimated uncertainty is about 3 K [16]. which is used as the equivalent physical temperature error.

To determine the overall uncertainty expected by GLOWS for various lens antenna losses, the additional accuracy error expected at 3 K equivalent physical temperature error is found by comparing the expected antenna noise temperatures 3 K apart for each loss. This error is added to the 0.62 K calibration stability of SMAP. The additional precision (Fig. 5.8) is found for the full illumination case at each loss and added to the 0.95 K precision of SMAP. The RSS of the two resultant terms is evaluated to find the overall expected uncertainty. Fig. 5.9 shows the results of this procedure.

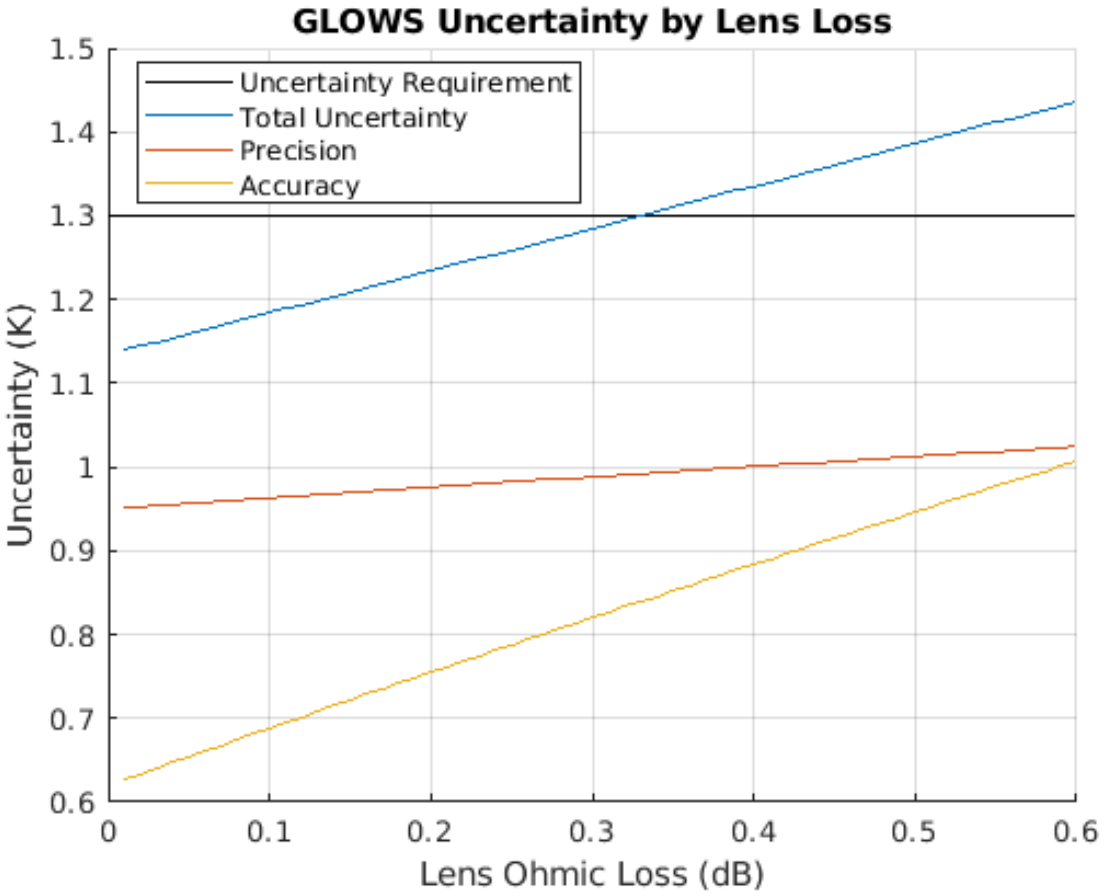

Figure 5.9: Overall uncertainty for various lens losses given a bulk temperature error of 3 K.

The results shown in Fig. 5.9 show that for a bulk physical temperature error of 3 K, the lens loss must be less than about 0.33 dB to maintain the total uncertainty (ΔT_B) of the radiometer below the required 1.3 K. The conservative working assumption has been that the GLOWS lens will achieve a loss of 0.5 dB. It should be possible, then, for the lens to achieve

a loss of 0.33 dB. If not, the temperature accuracy will need to be tightened. Repeating the procedure from before shows that if the physical temperature uncertainty drops to 2 K or 1 K, lens loss up to approximately 0.45 and 0.75 dB, respectively, can be tolerated.

5.7 Conclusions

Because of the increased loss involved in using a metamaterial lens, accounting for the additional noise due to self-emission by the lens is critical. The key factor in the accuracy of this calculation is the accuracy of the physical temperature used for each layer of the lens. Fortunately, the gradient across the lens turns out to be negligible (at least for the small gradients expected in typical application). Should the gradient increase (say because there is a shadow on the lens), then more precise knowledge of the temperature distribution is necessary to accurately represent and remove the self-emission of the lens. Ultimately, a bulk model of the temperature of the lens proves sufficient for achieving relatively low accuracy error if the lens has low loss. As the lens loss increases, the requirements on the bulk temperature accuracy tighten and vice versa. Ultimately, the requirements on the lens loss and the temperature accuracy to allow GLOWS to achieve requirements are tight, but they are within reason.

CHAPTER 6. CONCLUSION

6.1 Summary

In an effort to ensure that the GLOWS mission can successfully continue the SMAP mission, a unified framework for modeling and analyzing the performance of GLOWS has been presented. This framework has allowed for verification that GLOWS can meet SMAP mission requirements.

The backbone of much of the framework is the geometry modeling software. This has been consolidated and improved from several older programs. In some instances, the algorithms have been entirely redesigned or replaced. This software simplifies modeling and calculation of several key parameters in remote sensing observation, allowing for easy implementation of simulations.

Using the geometry software, the connection between instrument and measurement requirements was validated. The orbit was shown to be chosen perfectly to allow for consistent time of day measurements and the selection of a 1000 km swath width allows for a revisit period of 3 days over the whole Earth surface. The resolution requirements were shown to be met by both the radiometer and the radar. The connection between the radiometer and soil moisture uncertainty requirements was also justified. All of this proves that GLOWS can meet SMAP's performance requirements by essentially copying the design other than the antenna.

The effect of the antenna on the radiometer performance was then evaluated to ensure that the greater loss of the lens does not make meeting the radiometer uncertainty requirements impossible. The radar performance was not evaluated because to the radar, the slight added noise and increased loss are extremely manageable. In order to characterize the effects of the lens, a model was developed in which a bulk equivalent temperature for the whole antenna is defined based on the temperatures and losses of all layers of the lens. Ultimately,

there are tight requirements on the estimation of this equivalent temperature to prevent the overall radiometer uncertainty from exceeding the 1.3 K required. While these requirements are tight, it is still possible for GLOWS to meet them provided the lens is determined to achieve low enough loss.

6.2 Contributions

The contributions of this work are reiterated and expanded here:

1. Improvement of observational geometry modeling

   All of the observational geometry modeling software has been combined into one easy to use package with documentation. Several of the functions have also been improved for speed and/or accuracy. The package provides a solid foundation for space-based remote sensing simulation.

2. Verification that orbit and observation geometry meet mission requirements

3. Validation of the connection between soil moisture and brightness temperature uncertainties

   The GLOWS team wanted to independently verify that using SMAP mission parameters will achieve desired measurement requirements, which is accomplished in Chapter 4.

4. Development of a radiometric model of a lens antenna

   As far as the author is aware this is the first characterization of the effects of a lens antenna on a radiometer system because the setup has never been used before. The model was developed and analyzed to find the most simple viable model.

5. Determination that the radiometer can still meet performance requirements despite loss in antenna

   While the model shows that there is a tight trade-off between accuracy of lens physical temperature and lens loss, the GLOWS lens antenna should still be able to meet performance requirements of the mission.

6.3 Future Work

With the ongoing GLOWS design study, there are several aspects of the mission that require further work to build off of these findings including:

1. Development of a full-fledged GLOWS simulation

   While the geometry software developed in this work provides a solid foundation, GLOWS needs additional simulation programs to enable studies of the effects of various parameters throughout mission planning.

2. Development of a more accurate model of lens equivalent physical temperature and loss

   The accuracy and precision of the radiometer measurements depend to a large degree on the accuracy of the equivalent physical temperature used for the lens. Modeling this temperature depends on accurately characterizing the loss of the lens and calibrating the radiometer measurements (hopefully against concurrent SMAP data). This will be a key factor in the success of the GLOWS mission.

REFERENCES

[1] F. T. Ulaby and D. G. Long, *Microwave Radar and Radiometric Remote Sensing.* Ann Arbor: The University of Michigan Press, 2014. 1, 6, 7, 9, 12, 60

[2] D. Entekhabi, E. G. Njoku, P. E. O'Neill, K. H. Kellogg, W. T. Crow, W. N. Edelstein, J. K. Entin, S. D. Goodman, T. J. Jackson, J. Johnson, J. Kimball, J. R. Piepmeier, R. D. Koster, N. Martin, K. C. McDonald, M. Moghaddam, S. Moran, R. Reichle, J. C. Shi, M. W. Spencer, S. W. Thurman, L. Tsang, and J. Van Zyl, "The Soil Moisture Active Passive (SMAP) Mission," *Proceedings of the IEEE*, vol. 98, no. 5, pp. 704–716, May 2010, conference Name: Proceedings of the IEEE. 2, 13

[3] J. R. Piepmeier, P. Focardi, K. A. Horgan, J. Knuble, N. Ehsan, J. Lucey, C. Brambora, P. R. Brown, P. J. Hoffman, R. T. French, R. L. Mikhaylov, E.-Y. Kwack, E. M. Slimko, D. E. Dawson, D. Hudson, J. Peng, P. N. Mohammed, G. De Amici, A. P. Freedman, J. Medeiros, F. Sacks, R. Estep, M. W. Spencer, C. W. Chen, K. B. Wheeler, W. N. Edelstein, P. E. ONeill, and E. G. Njoku, "SMAP L-Band Microwave Radiometer: Instrument Design and First Year on Orbit," *IEEE Transactions on Geoscience and Remote Sensing*, vol. 55, no. 4, pp. 1954–1966, Apr. 2017, conference Name: IEEE Transactions on Geoscience and Remote Sensing. 2, 13, 17

[4] D. G. Long, M. J. Brodzik, and M. Hardman, "Enhanced-resolution SMAP soil moisture using image reconstruction," in *2017 IEEE International Geoscience and Remote Sensing Symposium (IGARSS)*, July 2017, pp. 2499–2502, iSSN: 2153-7003. 2

[5] D. Long, R. Bindlish, J. Piepmeier, G. De Amici, and M. Bailey, "Global L-band Observatory for Water Cycle Studies (GLOWS)," in *2021 IEEE International Geoscience and Remote Sensing Symposium IGARSS*, July 2021, pp. 7779–7782, iSSN: 2153-7003. 2, 3

[6] "SMAP Handbook." [Online]. Available: https://smap.jpl.nasa.gov/system/internal_resources/details/original/178_SMAP_Handbook_FINAL_1_JULY_2014_Web.pdf 15, 17, 18, 48, 49, 51

[7] D. G. Long and C.-Y. Chi, "Documentation for the NSCAT Simulation Program," Dec. 1988, jPL Internal Memo. 20

[8] I. R. Cole, "Modelling CPV," Jan. 2015. [Online]. Available: https://hdl.handle.net/2134/18050 29

[9] H. Vermeille, "Direct transformation from geocentric coordinates to geodetic coordinates," *Journal of Geodesy*, vol. 76, no. 8, pp. 451–454, Nov. 2002. [Online]. Available: http://link.springer.com/10.1007/s00190-002-0273-6 38

[10] M. Spencer, W.-Y. Tsai, and D. Long, "High-resolution measurements with a spaceborne pencil-beam scatterometer using combined range/Doppler discrimination techniques," *IEEE Transactions on Geoscience and Remote Sensing*, vol. 41, no. 3, pp. 567–581, Mar. 2003, conference Name: IEEE Transactions on Geoscience and Remote Sensing. 54, 55

[11] R. West, "Soil Moisture Active and Passive Mission (SMAP) L1B S0, L1C S0 Algorithm Theoretical Basis Document (ATBD)." 54

[12] P. O'Neill, R. Bindlish, S. Chan, J. Chaubell, E. Njoku, and T. Jackson, "Algorithm Theoretical Basis Document Level 2 & 3 Soil Moisture (Passive) Data Products," Aug. 2020. 56, 57, 58

[13] J. Brown, "An Exploration of Neural Networks in Enhanced Resolution Remote Sensing Products," Ph.D. dissertation, Brigham Young University, Provo, UT, 2019. [Online]. Available: https://scholarsarchive.byu.edu/etd/9113 57

[14] F. T. Ulaby, R. K. Moore, and A. K. Fung, *Microwave Remote Sensing: Active and Passive*, ser. Remote sensing. Reading, Mass: Addison-Wesley Pub. Co., Advanced Book Program/World Science Division, 1981, no. no. 2-[4]. 60

[15] M. Spencer, K. Wheeler, C. White, R. West, J. Piepmeier, D. Hudson, and J. Medeiros, "The Soil Moisture Active Passive (SMAP) mission L-Band radar/radiometer instrument," in *2010 IEEE International Geoscience and Remote Sensing Symposium*, July 2010, pp. 3240–3243, iSSN: 2153-7003. 68

[16] M. Bailey, personal communication, Feb. 2022. 68